Single Channel Properties of P2X$_2$ Purinoceptors

Shinghua Ding* and Frederick Sachs‡

From the *Department of Chemical Engineering and ‡Department of Physiology and Biophysics, State University of New York at Buffalo, Buffalo, New York 14214

ABSTRACT The single channel properties of cloned P2X$_2$ purinoceptors expressed in human embryonic kidney (HEK) 293 cells and *Xenopus* oocytes were studied in outside-out patches. The mean single channel current–voltage relationship exhibited inward rectification in symmetric solutions with a chord conductance of ~30 pS at −100 mV in 145 mM NaCl. The channel open state exhibited fast flickering with significant power beyond 10 kHz. Conformational changes, not ionic blockade, appeared responsible for the flickering. The equilibrium constant of Na$^+$ binding in the pore was ~150 mM at 0 mV and voltage dependent. The binding site appeared to be ~0.2 of the electrical distance from the extracellular surface. The mean channel current and the excess noise had the selectivity: K$^+$ > Rb$^+$ > Cs$^+$ > Na$^+$ > Li$^+$. ATP increased the probability of being open (P_o) to a maximum of 0.6 with an EC$_{50}$ of 11.2 μM and a Hill coefficient of 2.3. Lowering extracellular pH enhanced the apparent affinity of the channel for ATP with a pK$_a$ of ~7.9, but did not cause a proton block of the open channel. High pH slowed the rise time to steps of ATP without affecting the fall time. The mean single channel amplitude was independent of pH, but the excess noise increased with decreasing pH. Kinetic analysis showed that ATP shortened the mean closed time but did not affect the mean open time. Maximum likelihood kinetic fitting of idealized single channel currents at different ATP concentrations produced a model with four sequential closed states (three binding steps) branching to two open states that converged on a final closed state. The ATP association rates increased with the sequential binding of ATP showing that the binding sites are not independent, but positively cooperative. Partially liganded channels do not appear to open. The predicted P_o vs. ATP concentration closely matches the single channel current dose–response curve.

KEY WORDS: adenosine triphosphate • kinetics • permeation • selectivity • channel

introduction

P2X purinoceptors are ligand-gated cation channels that are activated by extracellular ATP and its analogues. These receptors exist in excitable and nonexcitable cells, including neurons, smooth and cardiac muscles, glands, astrocytes, microglia, and B lymphocytes (Nakazawa et al., 1990a; Bean, 1992; Walz et al., 1994; Bretschneider et al., 1995; Capiod, 1998; McQueen et al., 1998). During the past few years, seven P2X purinoceptor subunits (P2X$_1$–P2X$_7$) have been cloned (Brake et al., 1994; Valera et al., 1994; Bo et al., 1995; Lewis et al., 1995; Chen et al., 1995; Buell et al., 1996; Seguela et al., 1996; Soto et al., 1996; Surprenant et al., 1996; Wang et al., 1996; Rassendren et al., 1997b). The P2X family has a distinctive motif for ligand-gated ion channels, with each subunit containing two hydrophobic transmembrane domains (M1 and M2) joined by a large intervening hydrophilic extracellular loop (Brake et al., 1994). The cDNA of each receptor is ~2,000 bp in length and has a single open reading frame encoding ~400 amino acids. A comparison of the amino acid sequences of the seven members shows an overall similarity of 35–50% (Collo et al., 1996; North, 1996; Surprenant et al., 1996).

Dose–response analyses of the cloned receptors made with whole cell currents revealed a Hill coefficient larger than 1, suggesting that activation of the channel involves more than one agonist. This is consistent with experiments on the native receptors in PC12 cells and sensory neurons (Friel, 1988; Nakazawa et al., 1991; Bean, 1992; Ugur et al., 1997). Studies aimed at measuring the subunit stoichiometry predict that the naturally assembled form of P2X receptor channels contains three subunits (Nicke et al., 1998).

All of the P2X clones can be expressed in heterologous cells, such as HEK 293 cells and *Xenopus* oocytes. ATP is a potent agonist for all cloned P2X receptors, and the receptors are highly selective for ATP over most other adenosine derivatives. However, benzyl-ATP is 10-fold more potent than ATP in activating P2X$_7$ receptors (Surprenant et al., 1996). It is interesting to point out that α,β-methyl ATP is a poor agonist for the subtypes that do not show desensitization: P2X$_2$, P2X$_4$, P2X$_5$, P2X$_6$, and P2X$_7$, but is a potent agonist for P2X$_1$ and P2X$_3$ receptors that do desensitize.

Address correspondence to Frederick Sachs, Department of Physiology and Biophysics, 320 Cary Hall, State University of New York at Buffalo, Buffalo, NY 14214. Fax: 716-829-2028; E-mail: sachs@buffalo.edu

Most studies of cloned P2X receptors have focused on the primary structure and pharmacology based on whole cell currents, while only a small amount of work has been done on the single channel properties. Single channel currents from P2X$_1$ receptors expressed in *Xenopus* oocytes were reported to have a mean amplitude of ~ 2 pA at -140 mV and a chord conductance of 19 pS between -140 and -80 mV (Valera et al., 1994). The conductance for P2X$_1$, P2X$_2$, and P2X$_4$ channels expressed in Chinese hamster ovary cells were ~ 18, 21, and 9 pS, respectively, at -100 mV with 150 mM extracellular NaCl, but the openings of P2X$_3$ were not resolved (Evans, 1996).

To provide a firmer basis for further analysis of the P2X family, we have examined P2X$_2$ receptors at the single channel level. We have characterized the current–voltage (I–V)[1] relationships, cation selectivity of permeation, ATP sensitivity, proton modulation, and gating kinetics.

materials and methods

Expression Systems

P2X$_2$ receptors were expressed either in stably transfected human embryonic kidney 293 (HEK 293) cells or in *Xenopus* oocytes by mRNA injection (Rudy and Iverson, 1992). Since receptor expression is generally too high to obtain patches with only a single channel, we decreased the expression of the receptors in *Xenopus* oocytes by reducing the amount of mRNA to 25 ng, lowering the incubation temperature from 17° to 14°C, and shorting the incubation time to 16 h.

For electrophysiological experiments, HEK 293 cells were cultured at 37°C for 1–2 d after passage. The medium for HEK 293 cells contained 90% DMEM/F12, 10% heat inactivated fetal calf serum, and 300 μg/ml geneticin (G418). The media were adjusted to pH 7.35 with NaOH and sterilized by filtration. The incubation medium (ND96) for *Xenopus* oocytes contained (mM): 96 NaCl, 2 KCl, 1 MgCl$_2$, 1.8 CaCl$_2$, 5 HEPES, titrated to pH 7.5 with NaOH. All chemicals were purchased from Sigma Chemical Co.

Electrophysiology

We made patch clamp recordings from HEK 293 cells 1–2 d after passage and from *Xenopus* oocytes 16 h after injecting mRNA. Single channel currents from outside-out patches and whole cell currents were recorded at room temperature (Hamill et al., 1981). Recording pipettes, pulled from borosilicate glass (World Precision Instruments, Inc.) and coated with Sylgard, had resistances of 10–20 MΩ.

For recording from HEK 293 cells, the pipette solution contained (mM): 140 NaF, 5 NaCl, 11 EGTA, 10 HEPES, pH 7.4. The bath solution and control perfusion solutions were the same and contained (mM): 145 NaCl, 2 KCl, 1 MgCl$_2$, 1 CaCl$_2$, 11 glucose, 10 HEPES, pH 7.4. For *Xenopus* oocytes, the pipette solution contained 90 mM NaF instead of 140 mM NaF and other compo-

nents were the same as for HEK 293 cells; the bath and control perfusion solutions were the same as those used for HEK 293 cells except that they contained 100 instead of 145 mM NaCl. The patch perfusion solutions were the same as the bath solutions, except for modified divalent and ATP concentrations. Perfusate was driven by an ALA BPS-4 perfusion system (ALA Scientific Instruments). To investigate the cation selectivity of the channels, we substituted different cations for Na$^+$ ion in the perfusate. To investigate the affinity of Na$^+$ for the channel pore, we varied the extracellular NaCl concentration without compensation by other ions, while the pipette solution was kept constant. The resulting change of ionic strength caused the development of small liquid junction potentials between the bulk solution and the perfusate. We calculated these potentials according to the Henderson equation (Barry and Lynch, 1991). For solution exchanges from 100 to 150, 125, 100, 75, 50, and 25 mM NaCl, the junction potentials were -2.1, -1.2, 0, 2.5, 3.6, and 7.3 mV, respectively. Because these values are small compared with the holding potentials, we did not correct the membrane potential when we calculated the chord conductances.

Currents were recorded with a patch clamp amplifier (AXO-PATCH 200B; Axon Instruments), and stored on videotape using a digital data recorder (VR-10A; Instrutech Corp.). The data were low-pass filtered at 5–20 kHz bandwidth (-3 dB) and digitized at sampling intervals of 0.025–0.1 ms using a LabView data acquisition program (National Instruments).

Analysis

Amplitudes and excess channel noise. The mean amplitudes of single channel currents were determined by all-points amplitude histograms that were fit to a sum of two Gaussian distributions. Chord conductances were calculated assuming a reversal potential of 0 mV. The excess open channel noise (σ_{ex}) was computed as the root mean square (rms) difference between the variances of the open channel current and the shut channel current (Sivilotti et al., 1997).

The probability of the channel being open. P_o was defined as the ratio of open channel area (A_o) to the total area ($A_o + A_c$) in the all-points amplitude histogram:

$$P_o = \frac{A_o}{A_o + A_c}. \tag{1}$$

This calculation is insensitive to short events. In our initial analysis, we treated the channel as having two amplitude classes, open and closed. All rapid gating events associated with the open channel were treated as noise. Essentially we defined open as "not closed."

Power spectra. Power spectra, $S(f)$, were computed using the fast Fourier transform routine in LabView™. We used records of 50$\sim$100-ms duration associated with open and closed states. The power spectrum of the excess noise was obtained by subtracting the spectrum of the closed state spectrum from that of the open state. The spectra were fit with the sum of a Lorentzian plus a constant:

$$S(f) = \frac{S(0)}{1 + (f/f_c)^2} + S_1. \tag{2}$$

The rms noise, σ_L, from the Lorentzian component is:

$$\sigma_L = \sqrt{\frac{\pi}{2} f_c S(0)}. \tag{3}$$

---

[1]*Abbreviations used in this paper:* AIC, asymptotic information criterion; HEK cell, human embryonic kidney cell; I–V, current–voltage; rms, root mean square.

Thermal and shot noise. The thermal (or Johnson) and shot noise contributions were calculated according to Defelice (1981). The power spectra of thermal noise is white; i.e., it does not vary with frequency. Its value, S_{th}, is given by:

$$S_{th} = \frac{4 k_B T}{R},\qquad(4)$$

where $k_B T$ is Boltzmann's constant times the absolute temperature, and R is the equivalent resistance of the open channel. The rms noise in a bandwidth f is given by:

$$\sigma_{th} = \sqrt{\frac{4 k_B T f}{R}}.\qquad(5)$$

The power spectrum of shot noise, S_{sh}, is also white and given by:

$$S_{sh} = 2 q i,\qquad(6)$$

where q is the charge of an elementary charge carrier, and i is the single channel current amplitude. The rms amplitude of shot noise over bandwidth f is:

$$\sigma_{sh} = \sqrt{2 q i f}.\qquad(7)$$

Multiple conductance levels. We tried to see if there were discrete subconductance levels making up the open channel "buzz mode" by using a maximum-point likelihood method (MPL; www.qub.buffalo.edu) that use the Baum-Welch algorithm (Chung et al., 1990). While we did get convergence at four to six levels, these levels were not consistent among data from different patches, so at the present time we cannot confidently describe the substate structure.

Kinetic analysis. The single channel currents were idealized with a recursive Viterbi algorithm known as the "segmental k-means" algorithm (SKM; www.qub.buffalo.edu; Qin et al., 1996b). Idealization is dominated by the amplitude distribution, and therefore is essentially model independent. For simplicity, we used a two-state model for idealization: closed ↔ open (C ↔ O). The distributions of closed and open times were displayed as histograms with log distributed bin widths versus the square root of the event frequency (Sigworth and Sine, 1987). The mean open and closed times were simple averages from the idealized currents.

The rate constants of state models were obtained by using the maximal interval likelihood method with corrections for missed events (MIL; www.qub.buffalo.edu; Qin et al., 1996a). We used two strategies to fit the data: (a) individual fitting (i.e., fitting the data sets from each experimental condition individually), and (b) global fitting (i.e., fitting a group of data sets obtained under different experimental conditions). The first method produces an independent set of rate constants for each condition, but suffers from poor identifiability: a given model may not have unique rate constants. Global fitting improves identifiability by using a model with fewer parameters. We did both kinds of analysis of the data, and the results were consistent between the two methods of analysis, but global fitting permitted fitting more complicated models. For simplicity, we will emphasize the results of global fitting across ATP concentrations at the same voltage, or across voltages at the same ATP concentration. When we globally fit data from different ATP concentrations, we assumed that the association rates were proportional to concentration [i.e., $k_{ij} =$

$k_{ij}(0)$ [ATP], where $k_{ij}(0)$ is an intrinsic rate constant at the specified voltage], while the other rates were assumed to be independent of ATP. When we performed global fitting on data from different voltages at same ATP concentration, the rates were assumed to be exponential functions of voltage; i.e., $k_{ij} = k_{ij}(0)\exp(-z\delta_{ij}V/k_B T)$, where $k_{ij}(0)$ is the apparent rate constant at 0 mV and the specified ATP concentration, and $z\delta_{ij}$ is the effective sensing charge.

We used Akaike's asymptotic information criterion (AIC) to rank different kinetic models (Vandenberg and Horn, 1984; Horn, 1987):

$$AIC = 2\left[\sum_{j=1}^{n}\log(\text{maximum likelihood}) -\right.$$

$$(\text{number of free parameters of the model}) \times$$

$$\left.(\text{number of data sets}),\right]\qquad(8)$$

where j is the number of the data set. The model with a higher AIC is considered a better fit.

Simulation. We used Origin (Microcal Software, Inc.) and Scientist (MicroMath Scientific Software, Inc.) software to simulate and fit data.

r e s u l t s

Basic Features of Single Channel Currents

Fig. 1 A shows a typical single channel current, activated by 1.5 μM ATP at a membrane potential of −100 mV from a stably transfected HEK 293 cell. Channel openings appeared as flickery bursts with ill-defined conductance levels. There were a few clear closures and subconductance levels within a burst, but discrete levels could not be resolved from the all-points histogram (see Fig. 1 B). The spread of current levels was reflected by the much larger standard deviation of the open than the closed component, each of which could be fit reasonably well with a single Gaussian. In Fig. 1 B, the mean open current amplitude is 3.2 pA, equivalent to a chord conductance of 32 pS. The standard deviations of the open and closed histograms are 0.95 and 0.24 pA, respectively, so that the excess open channel noise σ_{ex} is 0.92 pA; i.e., 29% of the mean current amplitude. Since the mean is clearly less than the peak current, we obtained a closer estimate of the maximal open channel current by measuring the mean of extreme values. Comparing the upper 5% of the two distributions, the peak amplitude and conductance were 4.3 pA (Fig. 1 B, arrow) and 43 pS, respectively, a closer estimate of the maximum ion flux. However, for convenience in discussing later results, unless specified otherwise, "channel current" and "conductance" will refer to the mean rather than the peak values.

To further characterize the open channel noise, we followed the procedures of Sigworth (1985a) for noise analysis using differential power spectra. We compared
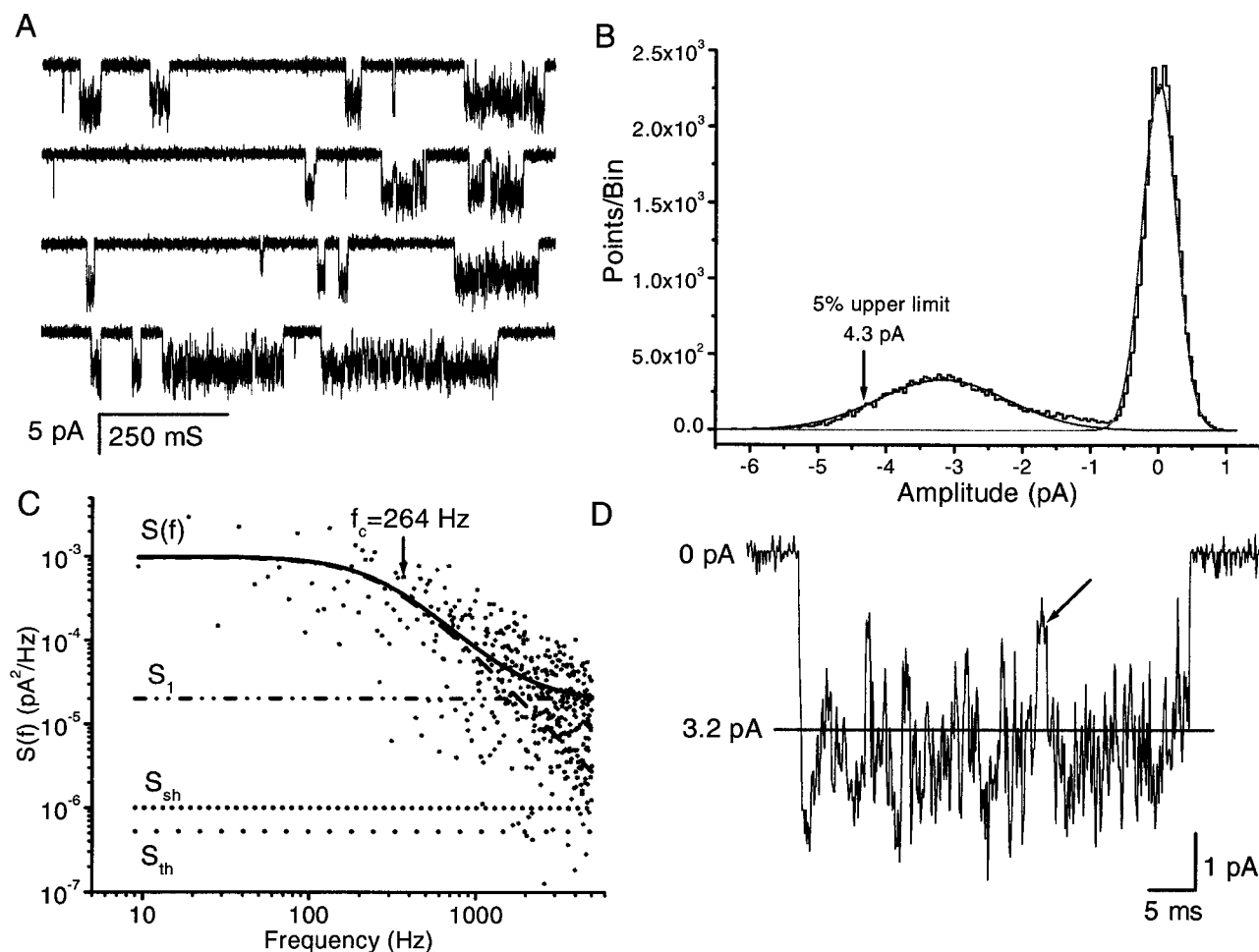
FIGURE 1. The general features of single channel currents from an outside-out patch of an HEK cell stably transfected with P2X$_2$ receptors. (A) Typical single channel current traces with inward current shown downward. The current was activated by 1.5 μM ATP at −100 mV, in the presence of 1 mM extracellular Mg^{2+} and Ca^{2+}. The data were low-pass filtered at 5 kHz and digitized at 10 kHz. There are large fluctuations in the open channel current. A distinct substate can be seen occasionally in some bursts (e.g., second trace, second opening burst; bottom trace, third opening burst). Due to their short lifetimes, these substates are not evident in the amplitude histogram (B). (B) The all-points amplitude histogram of single channel currents from A (0.05 pA/bin). The distribution was fit by a sum of two Gaussians (solid lines) with means of 0 and 3.2 pA. The standard deviation in the open state peak (0.95 pA) is much larger than that of the closed state peak (0.20 pA). (C) Comparison of the power spectrum of excess open channel fluctuations (solid line) with the expected thermal (dot line) and shot (short dot line) noises. Note that the amplitude of the open channel fluctuations is much larger than either thermal or shot noise. The solid line is a fit of the data to a Lorentzian with a cutoff at 264 Hz (dash dot line) plus a constant noted S$_1$ (dash dot dot line). The plotted spectrum is the average of three different spectra. (D) A higher time-resolution example of a burst at 5 kHz showing the general absence of easily discernible substates with one possible exception (arrow). The solid line is the mean current (3.2 pA).

the power spectra of excess open channel fluctuations with the expected thermal and shot noise (Fig. 1 C). The open channel spectrum was well fit with a Lorentzian with f_c = 264 Hz, equivalent to a relaxation time of 0.62 ms, plus a constant. This noise is much larger than the expected thermal or shot noise, suggesting that the fluctuations most likely arise from rapid conformational changes in the channel.

I–V Curve

Fig. 2 A shows the single channel currents recorded from HEK 293 cells activated by 2 μM ATP at different holding potentials using outside-out patches with sym-

metrical Na$^+$. The currents became small and noisy at positive holding potentials so that the unitary currents were not discernible. The single channel I–V curve (Fig. 2 B) exhibited a strong inward rectification similar to whole cell currents recorded under the same conditions (Fig. 3, A and B). The rapid fluctuation of current in the "open" state was maintained at all holding potentials.

Dose–Response Curve of Single Channel Currents

We were unsuccessful in obtaining outside-out patches containing only a single P2X$_2$ channel when the receptor was expressed in HEK 293 cells. However, we were
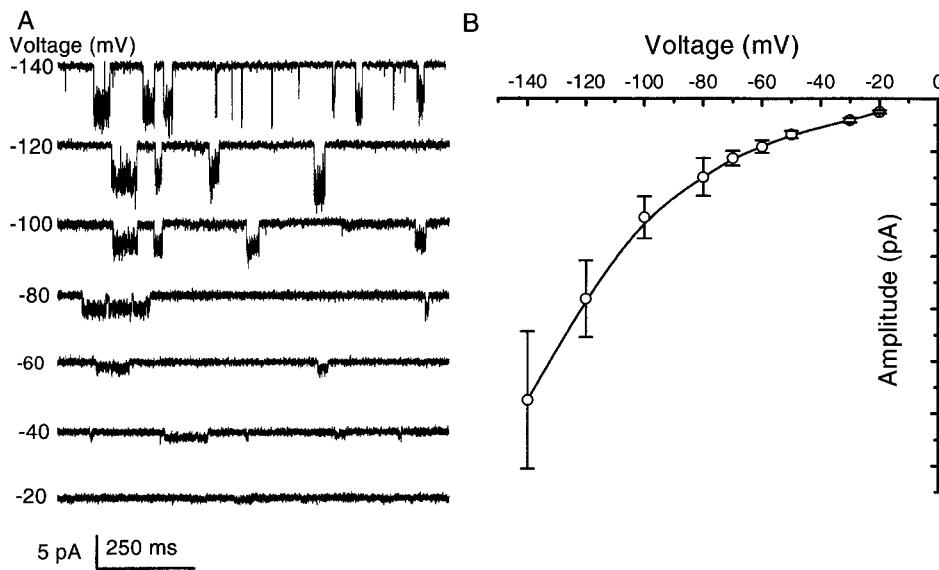
FIGURE 2. The current–voltage relationship of single channel currents. (A) Single channel currents of an outside-out patch from HEK 293 cells activated by 2 μM ATP (1 mM extracellular Mg^{2+} and Ca^{2+} at different membrane potentials, symmetrical Na^+ solutions containing 145 mM extracellular NaCl/145 mM intracellular NaF). The data were filtered at 5 kHz and digitized at 10 kHz. All of the current traces in this figure are from the same patch. (B) Mean I–V relationship of single channel currents. The error bars indicate the standard deviation of the single channel currents from the all-points histograms. The single channel I–V relationship shows strong inward rectification despite exposure to identical Na^+ solutions across the patch. The same result was obtained when single channel currents were recorded in the absence of Mg^{2+} and Ca^{2+}; therefore, divalent cations are not responsible for the rectification.
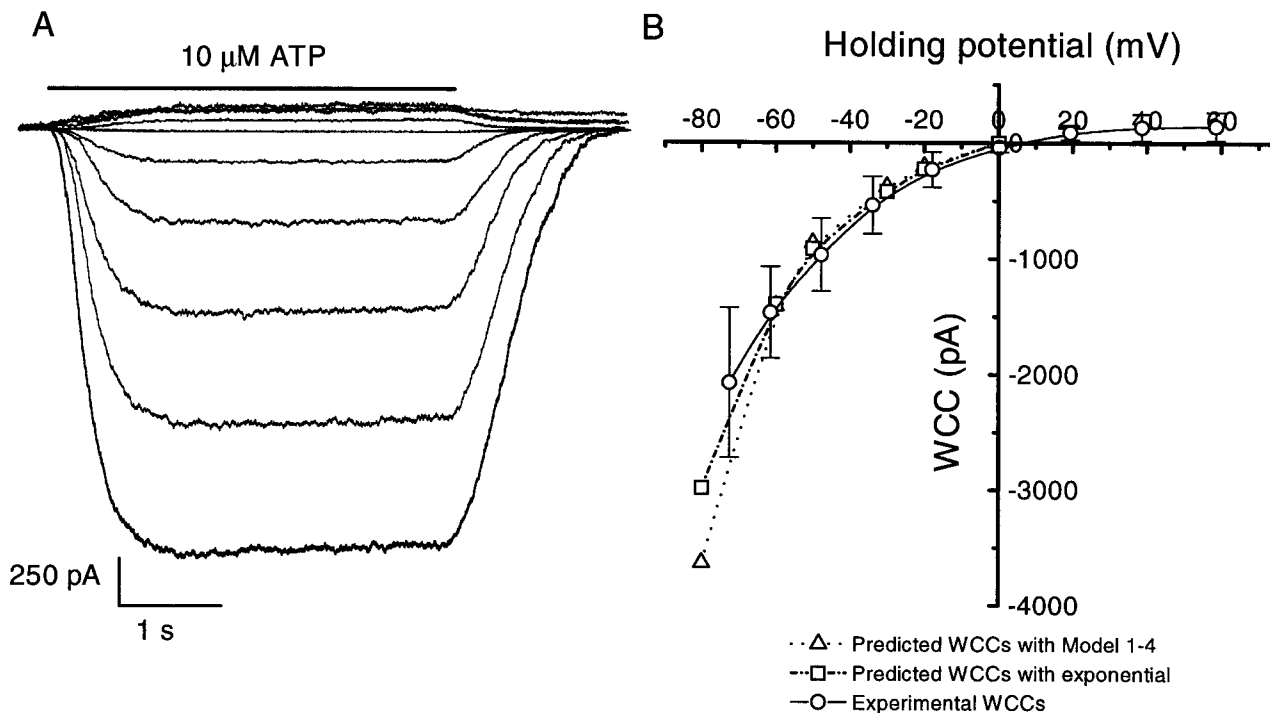

FIGURE 3. The current–voltage relationship of whole cell currents (WCCs). (A) Whole cell currents from an HEK 293 cell at different holding potentials: −100 to +80 mV at 20-mV intervals. Voltage drops from incomplete series resistance compensation were subtracted from the membrane potential. The currents were activated by 10 μM ATP in the presence of 1 mM extracellular Ca^{2+} with symmetrical Na^+ solutions: 145 mM extracellular NaCl/145 mM intracellular NaF. The data were filtered at 2 kHz and digitized at 5 kHz. (B) The mean WCCs (±SD) (O, $n = 5$) and predicted WCCs activated by 10 μM ATP. The I–V curve exhibits strong inward rectification, similar to the single channel currents shown in Fig. 2. The reversal potential was ~0 mV. The predicted WCCs were calculated using Eq. 15 where i (single channel amplitude) was taken from Fig. 2, and P_o from the calculations for Model 1-4 ($\triangle$) (Fig. 13), and Eq. 16 ($\square$) as a function of voltage. The number of channels was chosen so that the predicted WCC at −60 mV was equal to the experimental data. The predicted WCCs match reasonably well with the experimental data.
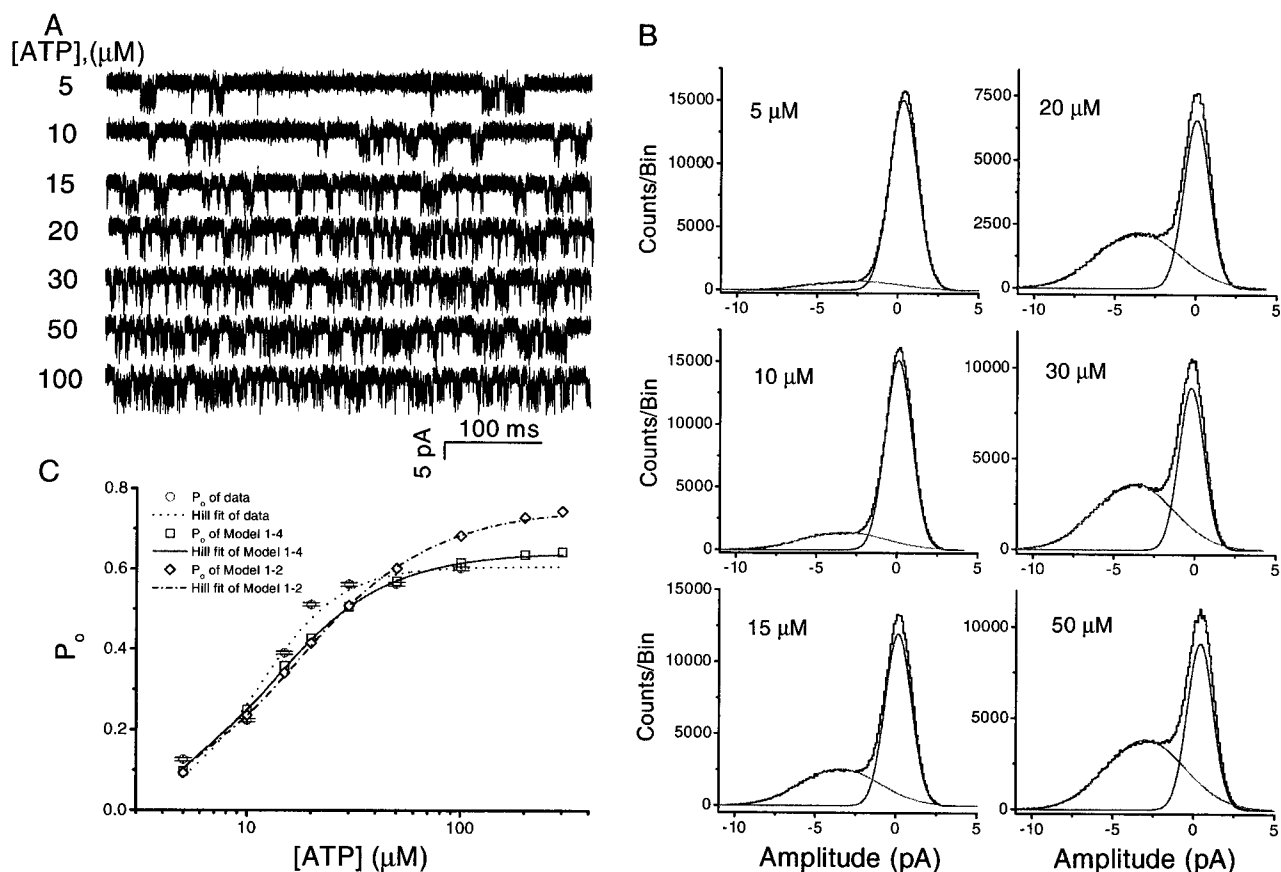
FIGURE 4. The effect of ATP concentration on single channel currents. (A) Single channel currents of P2X$_2$ receptors expressed in *Xenopus* oocytes activated by different concentrations of ATP in the absence of extracellular Ca^{2+} (-120 mV). The data were filtered at 20 kHz and sampled at 40 kHz. All of the current traces in this figure are from the same patch. (B) All-points amplitude histograms of the currents from A (0.05 pA/bin), with the distributions fit to the sum of two Gaussians. At this bandwidth, the excess channel noise was ~45% of the mean channel amplitude. (C) ATP dose–response curves. The probability of a channel being open is shown from experimental data (○) and simulated data generated by Fig. 13, Models 1-2 (◇) and 1-4 (□), as a function of ATP concentration. Fits of the data sets to the Hill equation are shown as dotted (experimental data), dash dot (Model 1-2), and solid (Model 1-4) lines. The Hill coefficient = 2.3, EC$_{50}$ = 11.0 μM, and maximum P_o = 0.61 for the experimental data, 1.5, 17.4 μM, and 0.74 for simulated data of Model 1-2, and 1.8, 13.3 μM, and 0.64 for simulated data of Model 1-4. All the experimental data were from same patch. The errors in the experimental P_o were estimated from the errors in the mean and standard deviation estimates reported by Origin when fitting the amplitude histograms to Gaussians.

able to obtain patches with a single channel from *Xenopus* oocytes provided we carefully controlled the amount of mRNA, and the time and temperature of incubation. Fig. 4 A shows the single channel currents from an outside-out patch activated by different concentrations of ATP. As expected, increasing the concentration of ATP increased P_o. The all-points histograms (Fig. 4 B) show that the average current and excess noise were independent of ATP concentration (i = 3.5 pA and σ_{ex} = 1.6 pA at -120 mV). Thus there is no indication that ATP is blocking the open channel. We calculated the probability of being open at each ATP concentration from the amplitude histograms using ratio of the open area to the total area (Fig. 4 C). The open probability saturated when the ATP concentration reached 30 μM. The dose–response curve was fitted by

the Hill equation with a Hill coefficient of 2.3, an EC$_{50}$ of 11.2 μM, and a maximal open probability of 0.61. The Hill coefficient and EC$_{50}$ are similar to those obtained from the dose–response curves of whole cell currents of our own data (not shown) and the literature (Brake et al., 1994), indicating that there are at least three subunits in a functional P2X$_2$ receptor ion channel. The data from this patch were very stable and used later in the comparison of kinetic models.

Na$^+$ Conduction through the Ion Channel

To investigate the affinity of Na$^+$ for the open channel, we measured single channel amplitudes at holding potentials of -80, -100, -120, -140 mV for extracellular NaCl concentrations of 10, 25, 50, 75, 100, 125, and 150
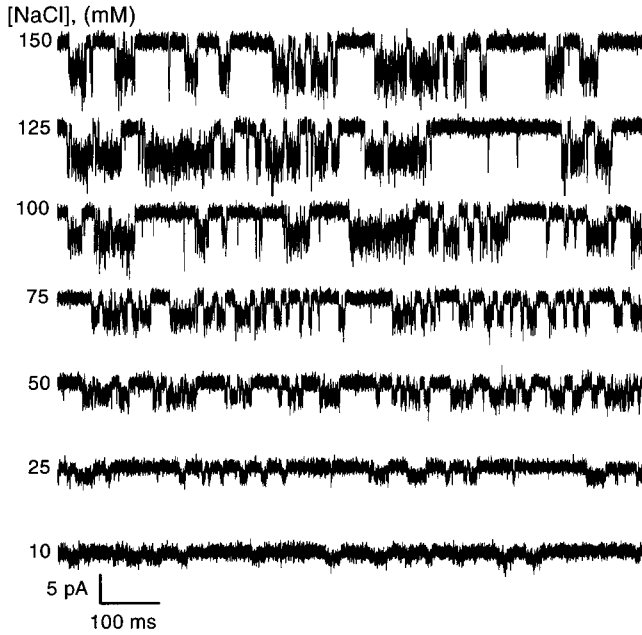
[NaCl], (mM)

FIGURE 5. The effect of extracellular NaCl concentration on the single channel current amplitude. Currents activated by 15 μM ATP were recorded from an outside-out patch from a *Xenopus* oocyte with different concentrations of NaCl without ionic substitution (different ionic strength) in the absence of Ca²⁺ at −120 mV. The data were digitized at 20 kHz and low pass filtered at 10 kHz.

mM. Fig. 5 shows single channel currents activated by 15 μM ATP at different extracellular Na⁺ concentrations with a holding potential of −120 mV (*Xenopus* oocyte). The amplitude increased with the concentration of NaCl but approached saturation at high Na⁺ levels. Because the solutions were asymmetric across the patch, we calculated the conductance with the driving force as the difference between the holding potential and the Nernst potential. The single channel chord conductance, γ, calculated this way is plotted as a function of Na⁺ concentration in Fig. 6 A. The conductance versus [NaCl] at each potential was well fit with the Michaelis-Menten equation (Hille, 1992):

$$\gamma = \frac{\gamma_{max}}{1 + K_s/[\text{NaCl}]},\qquad(9)$$

yielding K_s and γ_{max} at each voltage.

The equilibrium constant, K_s, increased with depolarization (Fig. 6 B). The relationship between K_s and holding potential can be described by a Boltzmann equation for a single binding site:

$$K_s(V) = K_s(0)\exp(-z\delta V/k_B T),\qquad(10)$$

where $K_s(0)$ is the dissociation constant at 0 mV, δ is the fractional electrical distance of the site from the extracellular surface, z is the valence of the permeating ion

(1 in this case), and $k_B T$ is Boltzmann's constant times absolute temperature (~25 mV at room temperature). The fitted values of $K_s(0)$ and δ were 148 mM and 0.21, respectively, so that a depolarization of 118 mV is required for an e-fold increase of K_s (Fig. 6 B). The Na⁺ binding site appears to be ~20% of the electrical distance from the extracellular surface, and is half saturated when exposed to 148 mM Na⁺ at 0 mV. The maximal conductance, γ_{max}, also increased with the potential as expected in a nearly linear part of the I–V curve (Fig. 6 C).

The Selectivity between Cations

The P2X₂ receptor ion channel is a nonselective cation channel; however, the conductance is different for different cations. We measured the single channel currents at −120 mV from HEK 293 cells using outside-out patches with NaF as the intracellular solution, and LiCl, NaCl, KCl, CsCl, and RbCl as the extracellular solutions (Fig. 7). From the currents obtained at −120 mV (Table I), the selectivity was K⁺ > Rb⁺ > Cs⁺ > Na⁺ > Li⁺. Although currents carried by the different cations had the same flickering behavior, the excess open channel noise, σ_{ex}, had a slightly different selectivity K⁺ ≅ Rb⁺ > Cs⁺ > Na⁺ > Li⁺. The relative noise, defined as σ_{ex}/i, was Rb⁺ ≅ Na⁺ ≅ Cs⁺ ≅ K⁺ > Li⁺. The difference in selectivity of the relative noise for Li⁺ suggests that it can affect the flickery kinetics. We compared σ_{ex} with the thermal, σ_{th}, and shot, σ_{sh}, noise (Table I). Again, σ_{th} and σ_{sh} were very small compared with σ_{ex}, and the ratio ($\sigma_{th} + \sigma_{sh}$) to σ_{ex} ranged from 8 to 14% depending on the ions. The relative noise caused by the open channel fluctuations, when corrected for thermal and shot noise $(\sigma^2_{ex} - \sigma^2_{th} - \sigma^2_{sh})^{1/2}/i$, followed the same cation sequence as σ_{ex}/i.

Effect of pH

The effect of pH on channel activation. The effect of extracellular pH on the channel currents is illustrated in Fig. 8 A. Multiple-channel outside-out currents activated by 2 μM ATP increased ~10-fold when pH was decreased from 8.3 to 6.8, and saturated with further decreases in pH (Fig. 8 B). The fluctuations in these multichannel currents at higher pH appeared to be dominated by the overlap of independent channels, so that at pH 8.3, where the mean current is small, single channel events were visible. At pH 6.3, the current saturated and the frequency of fluctuations increased dramatically, apparently dominated by the open channel noise. As is clear from the rise time of the currents, the activation rate decreased with increasing pH, and the fall time remained constant (Fig. 8 C). The potentiation of channel activity by protons is similar to the effect of increasing the ATP concentration, suggesting that protons may increase the affinity of the binding
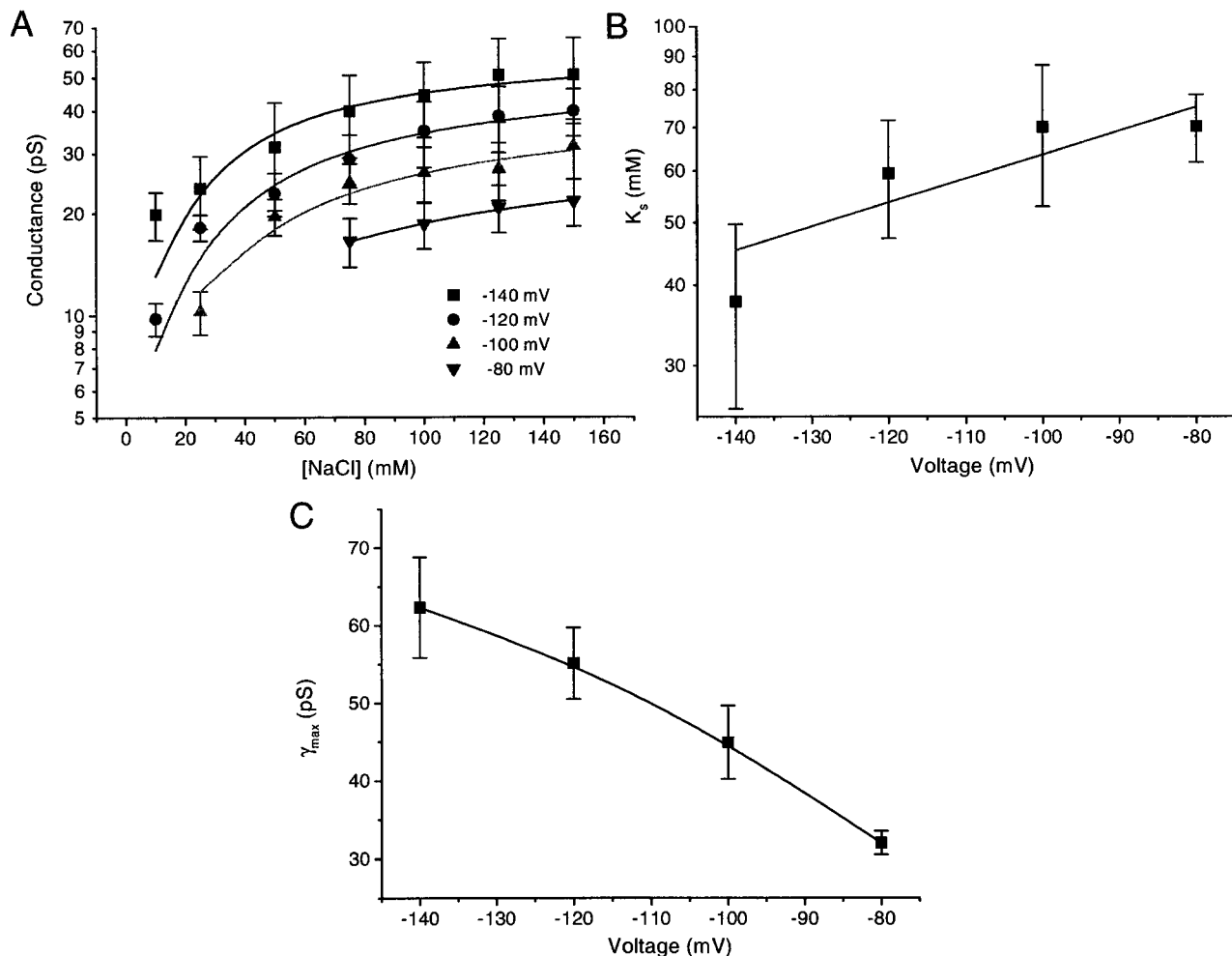
FIGURE 6. The affinity of Na$^+$ for the channels. (A). The relationship between the mean open channel conductance from Fig. 5 and the NaCl concentration at different voltages. The error bars are the standard deviations of the excess open channel noise. The solid line is a fit of Eq. 9. Note that at each concentration the driving force changes because of the change in Nernst potential. We have assumed K_s is dependent only on the holding potential and not the driving force. (B) The dependence of K_s on holding potential. The solid line was fit by the Boltzmann equation with $z = 1$, $\delta = 0.21$, and $K_s(0) = 148$ mM. A depolarization of 118 mV is required for an e-fold increase of K_s. The error bars are the parameter fitting errors from A. (C) The maximal conductance as a function of holding potential. The error bars are the fitting errors from A. The solid line is simply the connection of data. The conductance is approximately linear with the holding potential supporting the simple approximation of Eq. 9.

site for ATP. The pK$_a$ was ~7.9 and the Hill coefficient was 2.5, again suggesting that there are more than two subunits in the channel.

Effect of pH on single channel properties. The results above and published studies on the effect of pH were based on whole cell or multi-channel recordings (Li et al., 1996, 1997; King et al., 1997; Stoop et al., 1997; Wildman et al., 1998). To explore the possible effect of pH on gating and channel conductance, we examined the effect of pH on single channels. To obtain single channel activity from the stable cell lines, we exposed the patch to ATP for long times, so that run down reduced the number of active channels. Fig. 9 A shows these currents recorded at different values of extracellular pH. We measured the single channel amplitude and excess noise

from the all-points amplitude histograms. The mean amplitude of the current was independent of pH, but the excess open channel noise increased with decreasing pH (Table II). As visible in Fig. 9 A, the frequency of brief closures within open channel bursts appeared to increase as pH decreased. These interruptions were longer than the normal fast "flickery" behavior. It has been suggested that protons may block an open channel (Yellen, 1984). To further characterize this phenomenon, we computed the power spectra of the open channel fluctuations (Fig. 9 B), and fit them with a Lorentzian plus a constant (Eq. 3). The constant represents relaxations occurring at frequencies beyond our resolution.

The fits are illustrated in Fig. 9 B as solid lines. The Lorentzian represents a two-state relaxation process
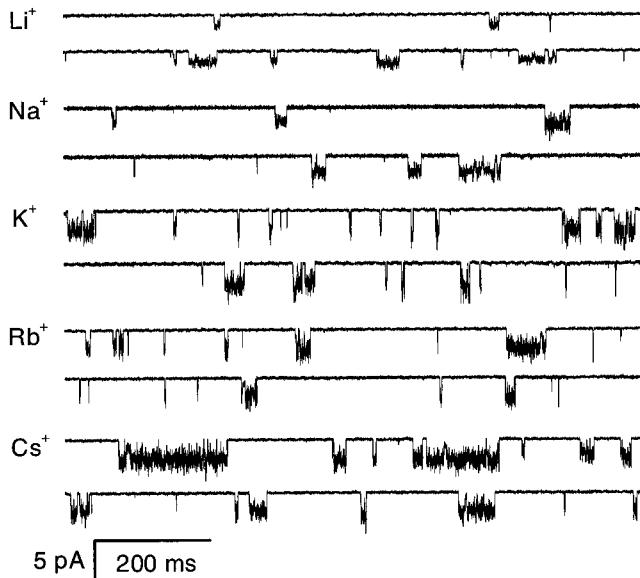
FIGURE 7. The effect of different permeant ions on the single channel currents. Single channel currents from HEK 293 cells at −120 mV activated by 2 μM ATP in the presence of 1 mM Mg^{2+} and Ca^{2+} from an outside-out patch. The data were filtered at 5 kHz and digitized at 10 kHz.

whose characteristic time constant τ is related to the corner frequency, f_c, by:

$$\tau = \frac{1}{2\pi f_c}. \tag{11}$$

Diffusional block of the open channel can be described as a two-state model (Scheme I), where O is the open state and C_b is the protonated-blocked state.

$$O + H^+ \underset{\beta}{\overset{\alpha}{\rightleftharpoons}} C_b \qquad \text{(SCHEME I)}$$
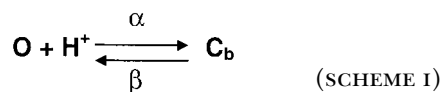
α and β are the blocking and unblocking rate constants. The relaxation time for this two-state process is related to the rate constants by:

$$\frac{1}{\tau} = 2\pi f_c = \alpha[H^+] + \beta. \tag{12}$$

The prediction of proton block is that f_c increases linearly with increasing proton concentration. However, our data show that f_c decreased with increasing proton concentration (Fig. 9 B). To further examine the possibility of proton block, we analyzed bursts kinetically using the maximum likelihood method with a two-state model. We fit the extracted α's and β's at different pH to an equation of the form:

$$\alpha = \alpha_0[H^+]^n, \tag{13}$$

where $\alpha_0 = 224 \ \mu M^{-0.33}s^{-1}$, $n_\alpha = 0.33$, $\beta_0 = 1{,}493$ $\mu M^{-0.16}s^{-1}$, and $n_\beta = 0.16$. Since α and β are not directly proportional to the proton concentration, a single site

<div style="text-align:center">

t a b l e i

The Effects of Different Cations on Open Channel Properties

</div>

Ion	Li⁺	Na⁺	K⁺	Rb⁺	Cs⁺
i (pA)	3.48	4.17	5.86	5.63	5.36
γ (pS)	29.0	34.8	48.8	46.9	44.7
σ_{ex} (pA)	0.92	1.40	1.90	1.96	1.79
σ_{ex}/i	0.264	0.336	0.324	0.348	0.334
σ_{th} (pA)	0.049	0.053	0.063	0.062	0.061
σ_{sh} (pA)	0.075	0.082	0.097	0.096	0.094
$(\sigma_{th} + \sigma_{sh})/\sigma_{ex}$	0.135	0.096	0.094	0.081	0.087
$(\sigma^2_{ex} - \sigma^2_{th} - \sigma^2_{sh})^{1/2}/i$	0.263	0.335	0.324	0.348	0.333

The currents were recorded at −120 mV. Liquid junction potentials were not corrected. γ is chord conductance, σ_{ex} excess open channel noise, σ_{th} thermal noise, and σ_{sh} shot noise.

model appears to be inappropriate. We speculate that we may be titrating several sites that display negative cooperativity. The effect of pH on the open channel is to modify the conformation of the channel rather than to provide a simple proton block. Table II summarizes the open channel properties at different pH. Remarkably, the effect of pH on the mean open channel current is negligible.

Kinetic Analysis with the Maximal-Interval Likelihood Method

To understand the kinetics of agonist binding and channel gating, we applied the maximum likelihood method to data from outside-out patches that were stable over time and ATP concentration (Fig. 4 A). We began by fitting simple noncyclic models using the maximum-likelihood interval analysis and used AIC ranking to select a preferred model. The analysis was hierarchical in the sense that we fit portions of the reaction scheme under restricted conditions, and then merged these models to create a full description. The kinetic description required: (a) the number of closed and open states, (b) the connections between states, and (c) the values of the rate constants between the states and their dependence on concentration and voltage.

Mean open and close times. The data was idealized into two classes: open and closed (see Fig. 10 A). We did not attempt to idealize the data making up the bulk of the flickery open channel activity since the amplitudes

<div style="text-align:center">

t a b l e ii

Summary of Open Channel Properties at Different pH

</div>

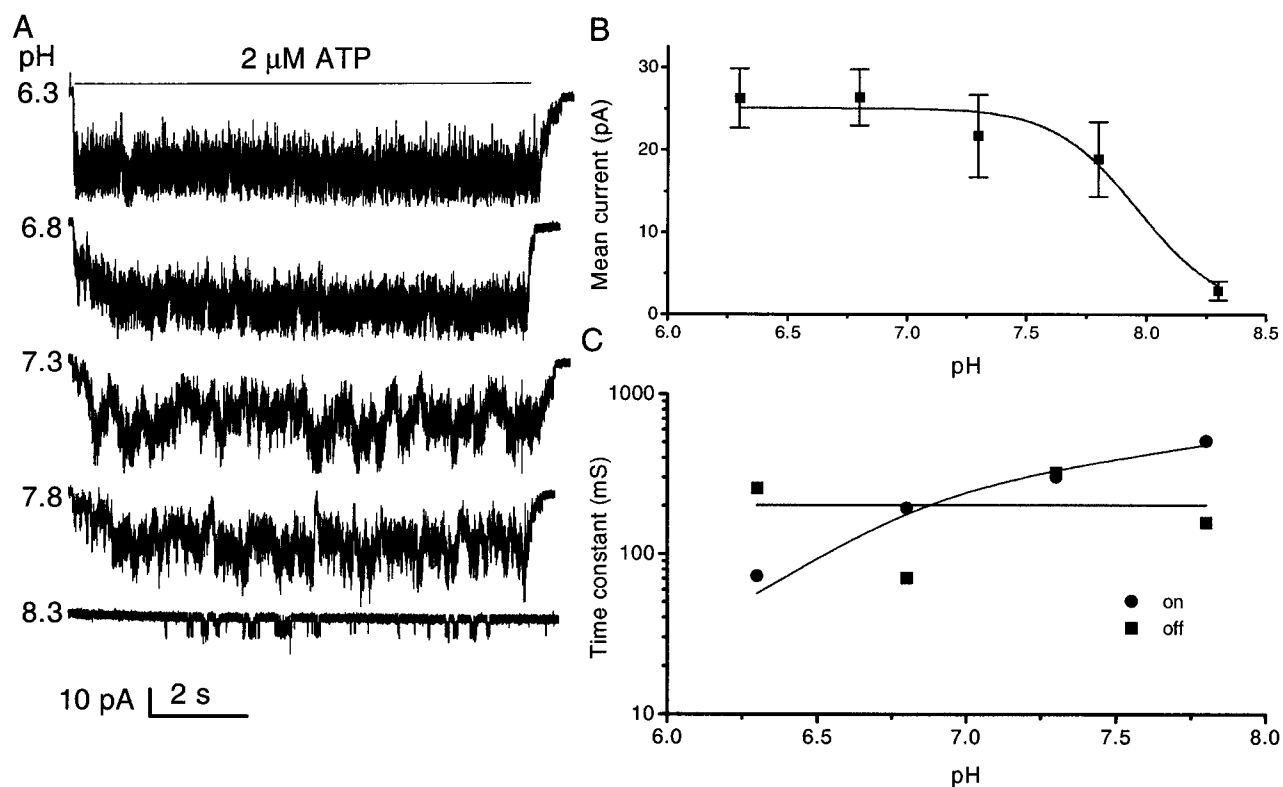| pH	Amplitude	σ_{ex}	f_c	τ	S_0	S_1	σ_L
	pA	pA	Hz	ms	$\times 10^3 \ pA^2/Hz$	$\times 10^5 \ pA^2/Hz$	pA
6.3	3.61	1.33	205	0.72	1.01	2.31	0.57
6.8	3.60	1.32	224	0.66	1.38	3.00	0.70
7.3	3.73	1.13	240	0.61	1.34	3.64	0.71
7.8	3.50	1.12	295	0.50	0.94	3.79	0.66
8.3	3.54	1.17	336	0.44	0.62	3.37	0.57

FIGURE 8. The effect of pH on the affinity of channel for ATP. (A) Multiple-channel currents from an outside-out patch of HEK cells at -120 mV and 2 μM ATP at different values of extracellular pH (0.3 mM extracellular Ca^{2+}). Note the increase in rise time with increasing pH. The data were low pass filtered at 5 kHz and digitized at 10 kHz. The horizontal bar indicates the duration of ATP application. (B) The effect of pH on mean patch current. The data were fitted by the Hill equation with a maximum mean current of 25.1 pA, an EC_{50} of pH 7.9 (pK_a), and a Hill coefficient of 2.5. The error bars are the standard deviation of the data and contain both open channel and gating noise. (C) The pH dependence of the rise and fall times. The time constants for rising (●) and falling (■) phase were obtained from fitting single exponential functions (solid lines) to multiple channel currents.

were uncertain, but instead defined open as a single conductance state possessing a lot of noise.

The probability of a channel being open increased with ATP, as shown in Fig. 4 C. This could result from an increase in mean open time, a decrease in mean closed time, or a combination. Fig. 10 B shows the mean open and closed times calculated from idealized single channel currents, and plotted as a function of ATP concentration. The mean closed time dramatically decreased with the increase in ATP and saturated at 30 μM, while the mean open time was not affected by ATP. The results indicate that ATP controls the rate at which the channel opens, but not the rate at which it closes.

Duration histograms. Fig. 10 C shows the open- and closed-time histograms from idealized single channel currents induced by different ATP concentrations (Fig. 10 A). The open-time histograms have two peaks and the closed-time histograms have at least three peaks at low concentration. When the ATP concentration was increased, the intermediate and long time constant peaks of the closed time distribution merged and only

two peaks were visible. These results indicate that the channel has at least three closed and two open states.

Kinetic model comparison. We made quantitative comparisons of various kinetic models to determine which model best described the behavior. The models were limited to three closed and two open states (of the same conductance), and at most 10 rate constants. These constraints proved necessary to obtain unique solutions during optimization. There are 98 unique models with that many states. Further constraints were imposed to simplify analysis. (a) We discarded models in which the unliganded states were open because we did not see any spontaneous openings in the absence of ATP. (b) Following traditional models for other ligand-gated channels, the closed states were connected so as to represent the binding of ATP. To evaluate the possible topologies, we used the program MSEARCH (www.qub.buffalo.edu) to compare the likelihood of all remaining models. The program evaluates all topologically unique models having a specified number of states of each conductance and optimizes the rate constants for each one. For this stage of the
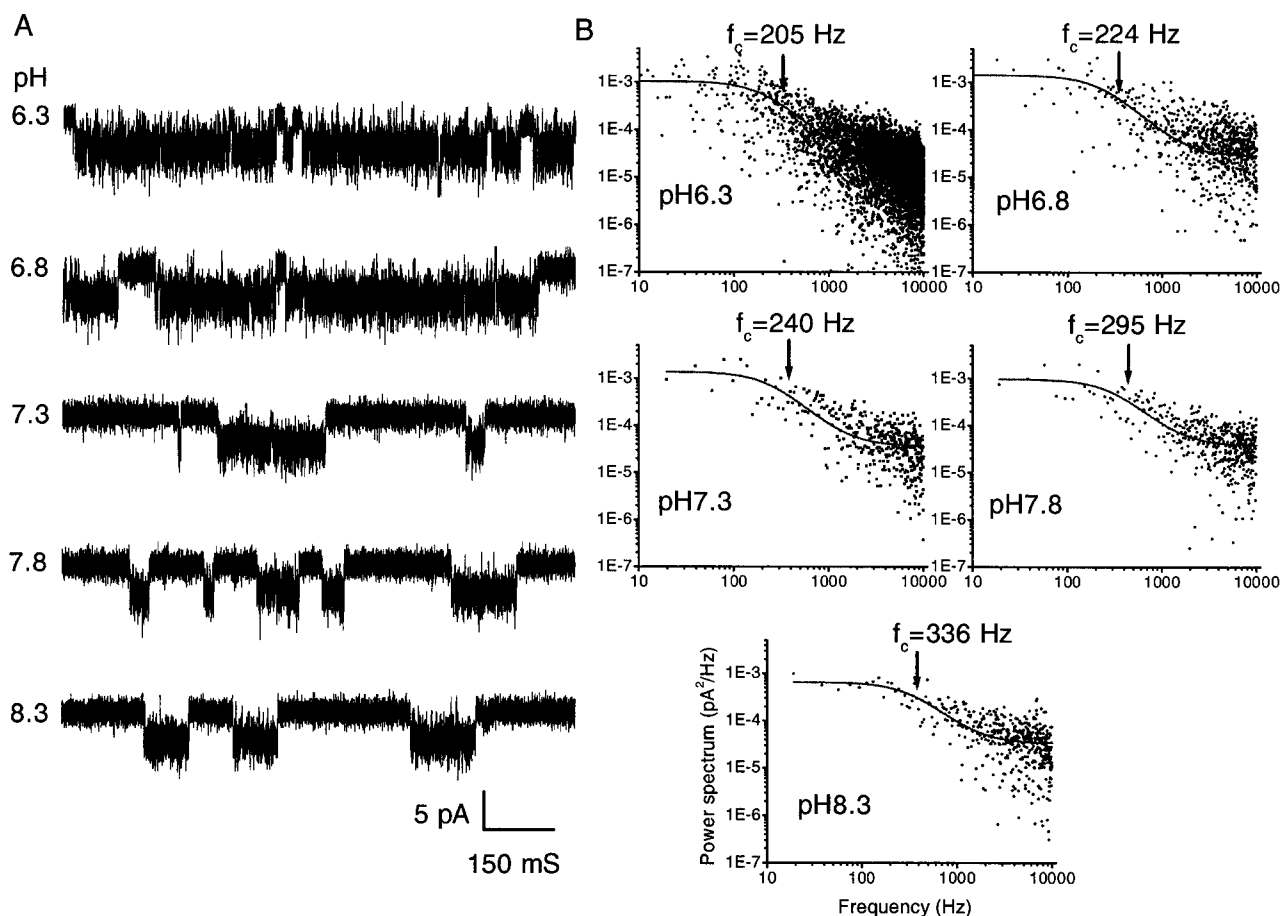
FIGURE 9. The effect of extracellular pH on single channel currents. (A) Currents recorded from an outside-out patch of an HEK 293 cell under the same experimental conditions as in Fig. 8 A. The data were low-pass filtered at 10 kHz and digitized at 20 kHz. (B) Differential power spectra of the open channel currents at different values of extracellular pH. The spectra were fit with the sum of a Lorentzian function plus a constant (solid line). The corner frequencies are indicated by the arrows. Plotted spectra are averages of three separate data segments.

analysis, we used three data sets obtained at 5, 10, and 15 μM ATP. We calculated the likelihood of each model by adding the log-likelihoods from each concentration. This is more a test of the topology of the models than a test of the optimal values of the rate constants since the rate constants will change over concentration, but the connectivity won't. Fig. 11 shows the eight kinetic models that converged on all data sets within 100 iterations. They are listed in the order of AIC rank.

To determine which model was best, we compared the log(maximum likelihood)s and AIC rankings (Table III). The likelihoods of Models 1, 2, and 3 (Fig. 11) are the same, but Model 3 has two more parameters and, hence, a lower AIC rank. Models 1 and 2 have the same number of parameters, likelihood, and AIC rank, so we can not tell the difference between them. Model 7 (Fig. 11) has a larger likelihood than Models 1 and 2; however, its AIC ranking is much lower because of the increased number of parameters. Model 8 (Fig. 11),

which has a partially liganded open state, has the smallest likelihood and lowest AIC rank. When Models 1 and 2 were compared across concentration, they were indistinguishable and, for simplicity in what follows, we arbitrarily selected Model 1. In both models, state C_1 is unliganded, C_2 and C_3 are liganded, and O_4 and O_5 are open. k_{12} and k_{23} are the agonist association rates, k_{21} and k_{32} are the agonist dissociation rates, k_{34} and k_{35} are the channel opening rates, and k_{43} and k_{53} are the channel closing rates.

The rate constants governing ATP binding and gating were solved by fitting across a range of ATP concentrations. Fig. 12 shows the rates from the model at bottom (from Fig. 11, Model 1) as a function of ATP concentration when the data from each concentration were fit independently. The association rates k_{12} and k_{23} showed a strong dependence on ATP concentration in the 5–20 μM range. However, when the ATP concentration was >20 μM, the rate constants appeared to satu-
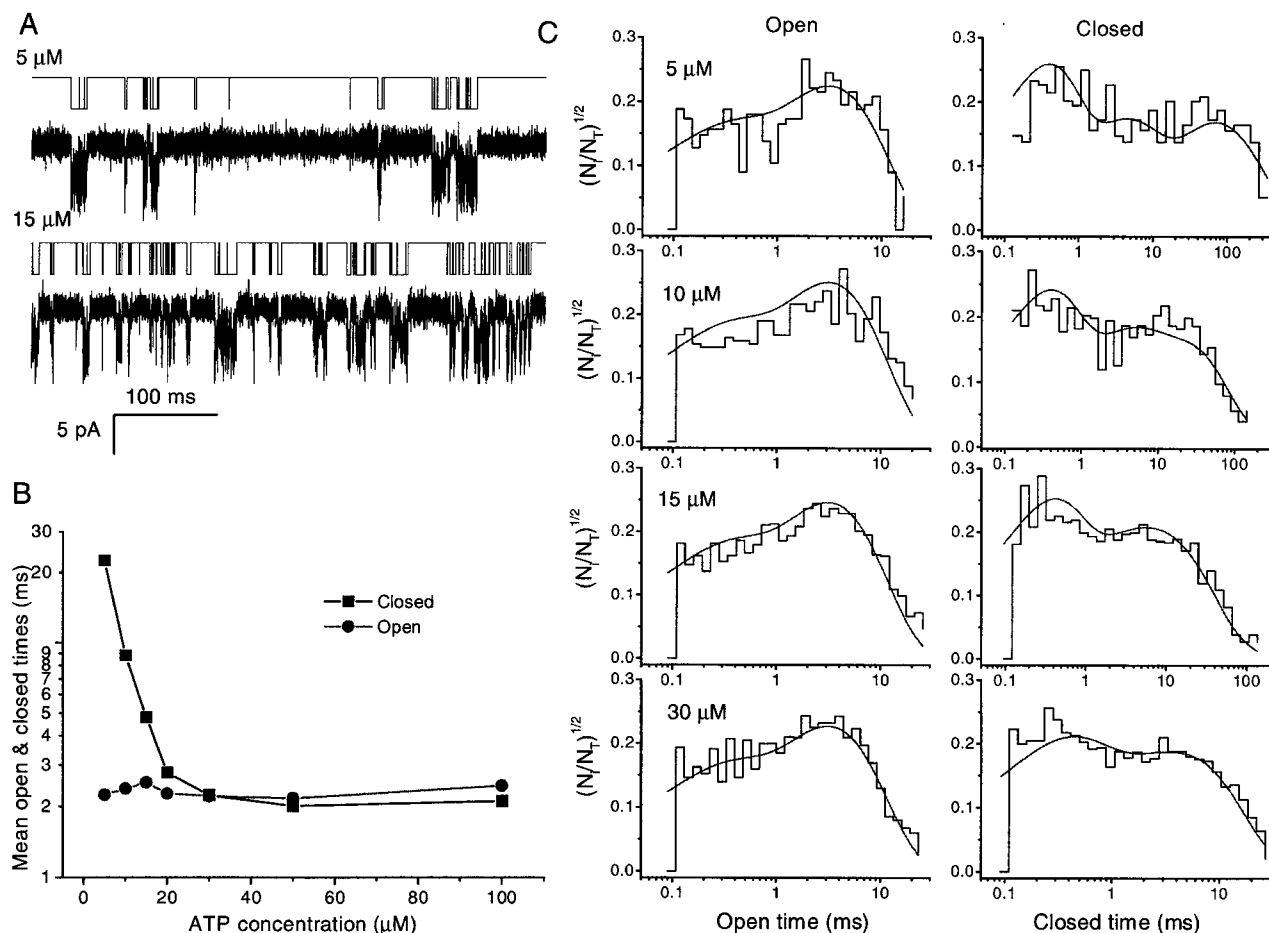
FIGURE 10. Idealization and open- and closed-interval duration histograms of single channel currents activated by different ATP concentrations (from the data in Fig. 4 A). (A) Examples of idealized single channel currents activated by 5 and 15 μM ATP. These data were recorded at 40 kHz and filtered at 20 kHz. Before idealization, the data were further filtered at 5 kHz using a Gaussian digital filter. The idealization was performed with the segmental k-means method based on a two-state model (see MATERIALS AND METHODS). (B) The mean open and closed times of single channel currents as a function of ATP concentration. (C) The open- and closed-time histograms of single channel currents activated by different concentrations of ATP. The solid lines are the predicted probability density functions for Fig. 13, Model 1-4, with rate constants determined by global fitting across concentrations (see Table VIII). N_i/N_T on the ordinate is the ratio of the number of events per bin to the total number of events.

rate and the error limits on the parameters increased. A concentration-driven rate should not saturate, but there are a few explanations. First, there may be a concentration-independent state not contained in the model. Second, k_{12} and k_{23} approach k_{35} at high ATP concentration, making k_{35} rate limiting and rendering the optimizer incapable of properly solving the model. Third, if k_{12} and k_{23} are linearly proportional to concentration, then the intrinsic rate constants of both k_{12} an k_{23} are $\sim 2 \times 10^7$ M^{-1}s^{-1}, which is approaching the diffusion limit.

We tested the first possibility by adding concentration-independent states to the model in Fig. 12, but that did not prevent the association rates from saturating. We tested the identifiability of the model by simulating the model across concentrations (SIMU;

www.qub.buffalo.edu) and attempting to extract the rate constants using maximal interval likelihood. Fitting the simulated data, we found that the estimated rate constants also saturated (see below) so that the correct model is not identifiable with data from a single concentration. As far as the diffusion limit providing a true saturation, further experiments are required to test that prediction. However, we currently believe that the apparent saturation is an artifact caused by the lack of identifiability of the model at high concentrations.

(Details of the test on the artifactual origin of saturating rates. We simulated data using Model 1 [Fig. 11], with the rate constants k_{12} and k_{23} increasing linearly with ATP in the 5–50 μM range. The intrinsic rate constants $k_{12}(0)$ and $k_{23}(0)$, obtained from the slope of k_{12} and k_{23} versus ATP from 5–30 μM (Fig. 12), were 14

Model 1 — states C_1, C_2, C_3, O_4, O_5 with rate constants k_{12}, k_{21}, k_{23}, k_{32}, k_{34}, k_{43}, k_{35}, k_{53}

Model 2 — states C_1, C_2, C_3, O_4, O_5 with rate constants k_{12}, k_{21}, k_{23}, k_{32}, k_{34}, k_{43}, k_{45}, k_{54}

Model 3 — states C_1, C_2, C_3, O_4, O_5 with rate constants k_{12}, k_{21}, k_{23}, k_{32}, k_{34}, k_{43}, k_{35}, k_{53}, k_{45}

Model 4 — states C_1, C_2, C_3, O_4, O_5 with rate constants k_{13}, k_{31}, k_{23}, k_{32}, k_{34}, k_{43}, k_{35}

Model 5 — states C_1, C_2, C_3, O_4, O_5 with rate constants k_{13}, k_{31}, k_{23}, k_{32}, k_{34}, k_{43}, k_{45}, k_{54}

Model 6 — states C_1, C_2, C_3, O_4, O_5 with rate constants k_{13}, k_{31}, k_{23}, k_{32}, k_{34}, k_{43}, k_{35}, k_{54}, k_{45}

Model 7 — states C_1, C_2, C_3, O_4, O_5 with rate constants k_{12}, k_{21}, k_{23}, k_{32}, k_{42}, k_{24}, k_{52}, k_{53}, k_{25}, k_{35}

Model 8 — states C_1, C_2, C_3, O_4, O_5 with rate constants k_{12}, k_{21}, k_{23}, k_{32}, k_{42}, k_{24}, k_{53}, k_{35}
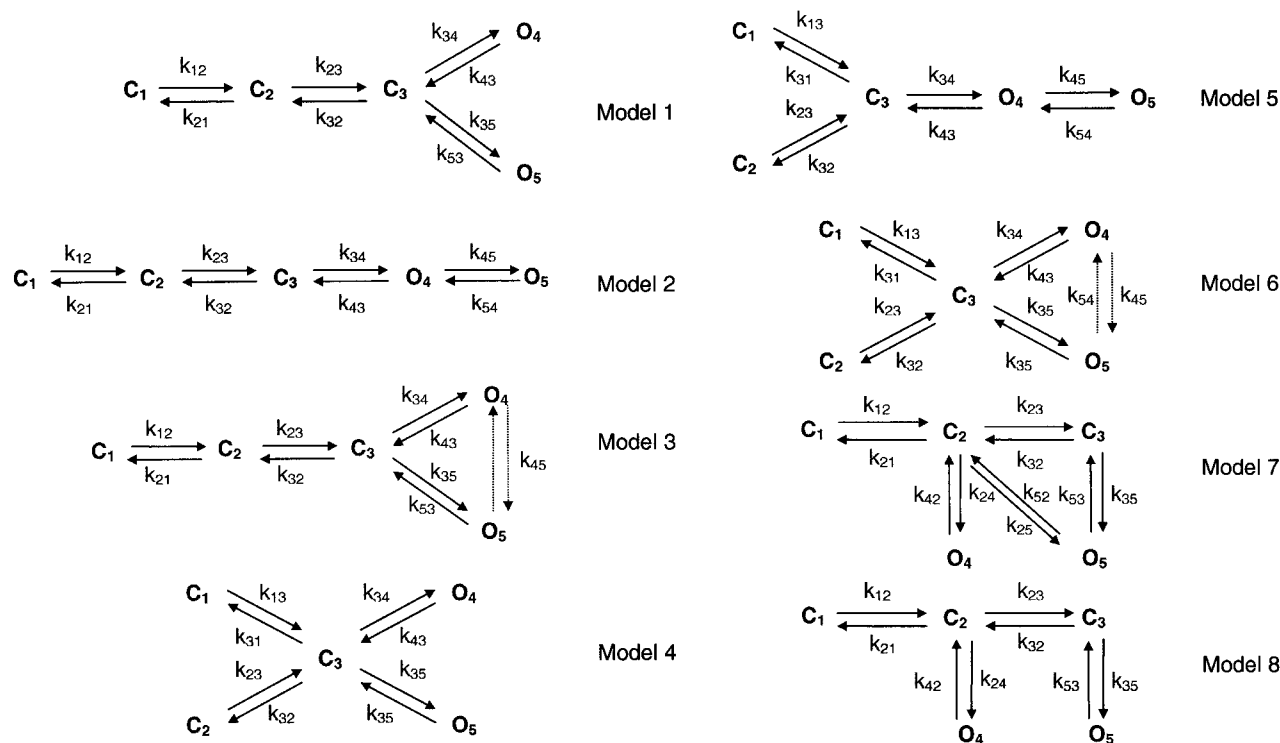
FIGURE 11. All models that converged during maximal likelihood estimation in the initial topology screen using the MSEARCH program. The relative likelihoods and AIC rankings of these models are listed in Table IV.

and 22 $\mu M^{-1}s^{-1}$, respectively. All other rate constants were made independent of ATP and set to values averaged across the data sets. We then analyzed the simulated data as if it were experimental data. The recovered rate constants were similar to the values used to simulate the data for ATP <20 μM. At higher ATP levels, however, the estimated values of k_{12} saturated and k_{21} even decreased. Large error limits also occurred in k_{12} and k_{21} at the high concentrations [Table IV]. Thus,

table iii
Model Comparison

Model	Relative log(Maximum likelihood)	AIC rank	Number of parameters
1	0	1	8
2	0	1	8
3	0	2	10
4	−0.6	3	8
5	−0.6	3	8
6	−0.6	4	10
7	+3.6	5	10
8	−46	5	8

Data sets from three different ATP concentrations were used for the calculation of likelihoods and AIC rankings. The lowest number of AIC rank is considered best.

Model 1 [Fig. 11] cannot uniquely fit data at single high ATP concentration.)

To improve identifiability, we fit the data simultaneously across all concentrations. Such global fitting makes the likelihood surface steeper (Qin et al., 1996a). We assumed that the association rate constants were proportional to the ATP concentration, and the other rate constants were independent of ATP (see MA-TERIALS AND METHODS). This time, the rate constants derived from global fitting of simulated data were very close to the values used for simulation (Table V). The results of global fitting to the experimental data are listed in Table VI. It is worth noting that the second ATP association rate constant, $k_{23}(0)$, is larger than the first, $k_{12}(0)$. This result shows that the binding sites are not independent, but that binding to one site modifies binding to the other. With independent sites, the association rate should decrease as the number of free sites decreases. The conclusion is quite model independent; for every model we tested, the association rates increased with proximity to the open state (see below).

Model simplification and expansion. As ATP concentration increased, the three peaks in the closed time duration histograms became two (Fig. 10 C), suggesting that at high ATP concentration, Model 1 (Fig. 11) could be simplified by removal of state C_1 (Fig. 13, Model 1-1). When we fit the kinetics of high concentrations of ATP
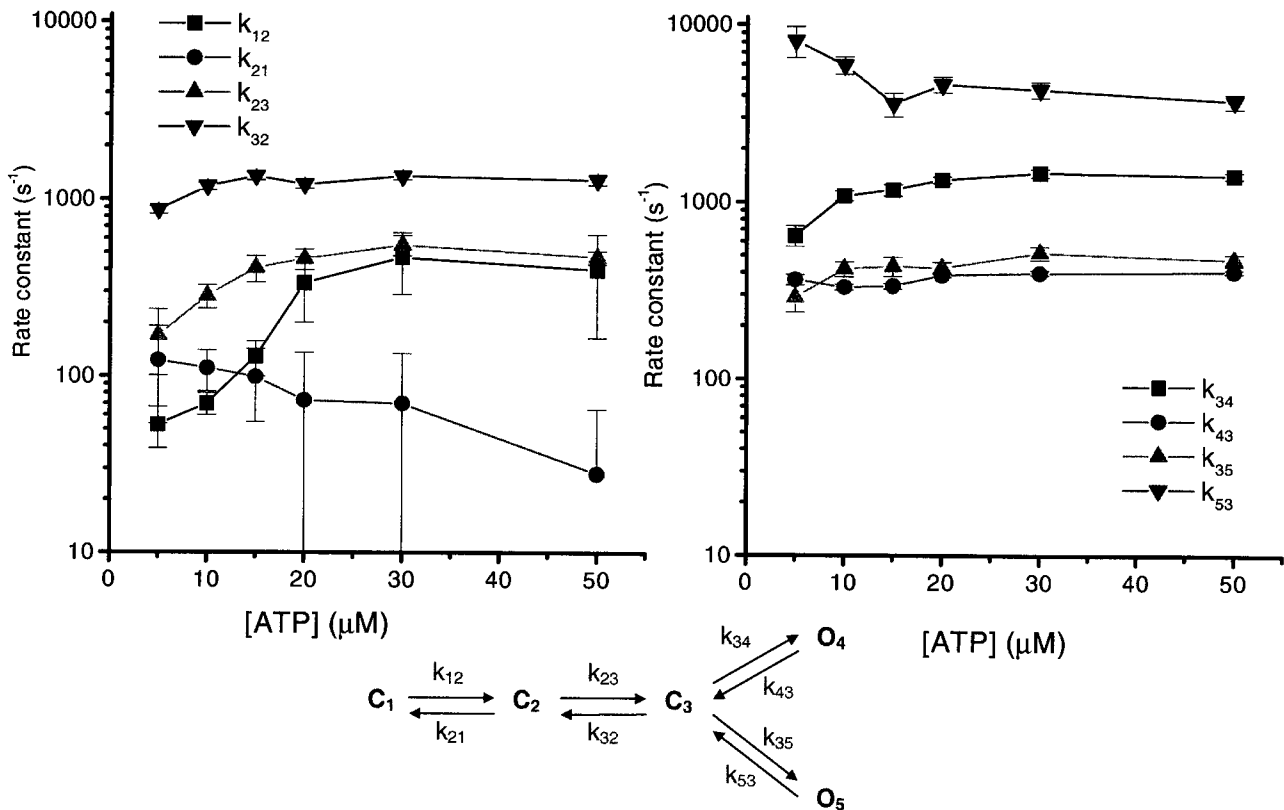
FIGURE 12. The effect of ATP concentration on the rate constants near the open states. The rate constants are based on kinetic Model 1 (shown at bottom), with each data set fit separately. Missed events were corrected by imposing a dead time of 0.05 ms. k_{12} and k_{23} are the most sensitive to the concentration of ATP, increasing over the range from 5 to 20 μM, and saturating at higher concentrations. The rate constants are plotted in two panels to avoid overlap (the scales in both plots are identical).

by Model 1 and Model 1-1, the likelihoods were equal. Thus, at high ATP, k_{12} gets so fast that C_1 is rarely occupied and Model 1-1 is sufficient to describe the kinetics. However, a large difference in maximum likelihoods arose when we fitted Models 1 and 1-1 to the data at low concentrations of ATP. Model 1-1 can well describe the kinetics of single channel currents of high ATP, but not low.

Our model has only two binding steps. The fact that the P_o curve has a Hill coefficient of 2.3 suggests that there are at least three binding sites in the P2X$_2$ channel. Since it is a homomer, this implies that three or more subunits are needed to form the channel. A more realistic model should have at least one additional partially liganded closed state (Fig. 13, Model 1-2).

The rate constants from Model 1-2 (Fig. 13) are shown in Table VI. Again in this model, the first ATP binding step speeds up the second one. The transition rates near the open state are similar between Model 1 (Fig. 11) and Model 1-2. While Model 1-2 has two more free parameters than Model 1, it has 5.4 units higher likelihood so that Model 1-2 is preferred (see Table VIII). The predicted P_o as a function of ATP concentra-

tion is plotted in Fig. 4 C (◇) and fit with the Hill equation with a Hill coefficient of 1.5, an EC_{50} of 17.4 μM, and maximal P_o of 0.74. However, compared with the experimental data, the EC_{50} and maximal P_o are too large and the Hill coefficient too small. These discrepancies can be reduced by connecting an ATP-independent closed state to the open states. Additional evidence for this closed state comes from the closed time histogram that has two components at saturating ATP (Fig. 10 C). Adding a closed state to the right of the open states in Model 1-2 produces Model 1-4 (Fig. 13). This modification corrects the prediction of the dose–response curve. Similarly, adding one more closed state to Model 1 produces Model 1-3 (Fig. 13).

Constraining Models 1-3 and 1-4 (Fig. 13) with detailed balance in the loops, and globally fitting the data from 5 to 50 μM ATP, we obtained rate constants with small error limits (Table VII). The relative likelihoods and the AIC ranking of Model 1 (Fig. 11) and its expanded versions, Models 1-2, 1-3, and 1-4 (Fig. 13) are listed in Table VIII. Models 1-3 and 1-4, which contain loops, have much higher likelihoods than Model 1 or 1-2. Model 1-4 has the highest AIC rank, and therefore is

table iv

Comparison of Simulation Values and Fitted Values of Rate Constants from Individual Fitting Based on Model 1 (Fig. 11)

[ATP]	5	10	15	20	30	50
μM						
k_{12} Simulation	70	140	210	280	420	700
Fitted	70 ± 17	146 ± 39	168 ± 99	203 ± 123	107 ± 85	192 ± 160
k_{21} Simulation	95	95	95	95	95	95
Fitted	124 ± 60	121 ± 70	42 ± 55	39 ± 39	5 ± 9	5 ± 9
k_{23} Simulation	110	220	330	440	660	1100
Fitted	135 ± 38	203 ± 51	236 ± 49	316 ± 54	424 ± 43	726 ± 71
k_{32} Simulation	1192	1192	1192	1192	1192	1192
Fitted	985 ± 130	902 ± 106	899 ± 96	867 ± 87	729 ± 81	662 ± 93
k_{34} Simulation	1145	1145	1145	1145	1145	1145
Fitted	922 ± 100	978 ± 72	964 ± 65	983 ± 56	916 ± 48	896 ± 45
k_{43} Simulation	365	365	365	365	365	365
Fitted	354 ± 22	358 ± 15	356 ± 13	354 ± 11	355 ± 10	351 ± 9
k_{35} Simulation	418	418	418	418	418	418
Fitted	307 ± 55	326 ± 39	321 ± 34	325 ± 31	293 ± 26	288 ± 24
k_{53} Simulation	5335	5335	5335	5335	5335	5335
Fitted	4795 ± 1060	5494 ± 810	4957 ± 653	4857 ± 540	4750 ± 487	4673 ± 450

$k_{12} = k_{12}(0)$ [ATP] and $k_{23} = k_{23}(0)$ [ATP]. $k_{12}(0)$ and $k_{23}(0)$ are 14 and 22 $\mu M^{-1}s^{-1}$, respectively. All rate constants have units of s^{-1}. Simulation values are rate constants used to simulate single channel currents. Fitted values are the rate constants obtained from maximal likelihood analysis of simulated data, using Model 1. Missed events were corrected by imposing a dead time of 0.05 ms.

the preferred model. The rate constants are listed in Table VI and VII. The transition rates near the open states for Models 1 and 1-2, and Models 1-3 and 1-4 are very similar, supporting the hierarchical approach. The predicted probability densities for the open and closed lifetimes of Model 1-4 are shown in Fig. 10 C and match the histograms reasonably well. Again, we found that the ATP association rate constants increased with proximity to the open states: $k_{12}(0) < k_{23}(0) < k_{34}(0)$. This is opposite to what would be expected from independent subunits. Each binding step makes the next faster. This cooperativity of binding appears model independent since all models tested had the same trend. From

the Eyring model for the rates, the energy landscape for the whole reaction is shown in Fig. 14.

The kinetic model fits the single channel data quite well. In Fig. 4 C, the predicted P_o (□) from Model 1-4 (Fig. 13) and its fit to the Hill equation (solid line) are plotted as a function of ATP. The maximal P_o (0.64) and EC_{50} (13.3 μM) are close to those of the experimental data, although the Hill coefficient (1.8) is slightly smaller. These values are much closer to experi-

table v

Comparison of Simulation Values and Fitted Values of Rate Constants from Global Fitting Based on Model 1 (Fig. 11)

Rate constant	Simulation value	Fitted value
$k_{12}(0)$, ($\mu M^{-1}s^{-1}$)	14	13.9 ± 2.0
k_{21}, (s^{-1})	95	92 ± 20
$k_{23}(0)$, ($\mu M^{-1}s^{-1}$)	22	18.6 ± 1.0
k_{32}, (s^{-1})	1192	890 ± 38
k_{34}, (s^{-1})	1145	978 ± 20
k_{43}, (s^{-1})	365	356 ± 4
k_{35}, (s^{-1})	418	319 ± 11
k_{53}, (s^{-1})	5335	4793 ± 208

Simulation values are the rate constants used to simulate single channel currents. Fitted values are the values of rate constants obtained from maximum likelihood analysis of simulated data, using Model 1. Missed events were corrected by imposing a dead time of 0.05 ms.

table vi

Rate Constants Obtained from Global Fitting Based on Models 1 and 1-2 (Figs. 11 and 13, respectively)

Model 1		Model 1-2	
Rate constant	Value	Rate constant	Value
		$k_{12}(0)$, ($\mu M^{-1}s^{-1}$)	4.4 ± 1.6
		k_{21}, (s^{-1})	10.7 ± 7.5
$k_{12}(0)$, ($\mu M^{-1}s^{-1}$)	7.6 ± 0.7	$k_{23}(0)$, ($\mu M^{-1}s^{-1}$)	11.2 ± 1.7
k_{21}, (s^{-1})	54.2 ± 10.7	k_{32}, (s^{-1})	70.2 ± 12.7
$k_{23}(0)$, ($\mu M^{-1}s^{-1}$)	20.4 ± 1.0	$k_{34}(0)$, ($\mu M^{-1}s^{-1}$)	20.7 ± 1.0
k_{32}, (s^{-1})	1191 ± 46	k_{43}, (s^{-1})	1195 ± 46
k_{34}, (s^{-1})	1264 ± 31	k_{45}, (s^{-1})	1263 ± 31
k_{43}, (s^{-1})	374 ± 5	k_{54}, (s^{-1})	374 ± 5
k_{35}, (s^{-1})	450 ± 18	k_{46}, (s^{-1})	450 ± 18
k_{53}, (s^{-1})	4474 ± 238	k_{64}, (s^{-1})	4474 ± 240

Single channel currents activated by 5, 10, 15, 20, 30, and 50 μM ATP were used for global fitting. The rate constants near the open states were very close between the two models. Missed events were corrected by imposing a dead time of 0.05 ms.

Model 1-1

$$C_2 \underset{k_{32}}{\overset{k_{23}}{\rightleftharpoons}} C_3 \underset{k_{43}}{\overset{k_{34}}{\rightleftharpoons}} O_4 \qquad C_3 \underset{k_{53}}{\overset{k_{35}}{\rightleftharpoons}} O_5$$

Model 1-2

$$C_1 \underset{k_{21}}{\overset{k_{12}}{\rightleftharpoons}} C_2 \underset{k_{32}}{\overset{k_{23}}{\rightleftharpoons}} C_3 \underset{k_{43}}{\overset{k_{34}}{\rightleftharpoons}} C_4 \underset{k_{54}}{\overset{k_{45}}{\rightleftharpoons}} O_5 \qquad C_4 \underset{k_{64}}{\overset{k_{46}}{\rightleftharpoons}} O_6$$

Model 1-3

$$C_1 \underset{k_{21}}{\overset{k_{12}}{\rightleftharpoons}} C_2 \underset{k_{32}}{\overset{k_{23}}{\rightleftharpoons}} C_3 \;\; k_{34}, k_{43}, O_4, k_{46}, k_{64}, C_6, k_{35}, k_{53}, k_{56}, k_{65}, O_5$$

Model 1-4

$$C_1 \underset{k_{21}}{\overset{k_{12}}{\rightleftharpoons}} C_2 \underset{k_{32}}{\overset{k_{23}}{\rightleftharpoons}} C_3 \underset{k_{43}}{\overset{k_{34}}{\rightleftharpoons}} C_4 \;\; k_{45}, k_{54}, O_5, k_{57}, k_{75}, C_7, k_{46}, k_{64}, O_6, k_{67}, k_{76}$$

Model 1-5

$$C_1 \underset{k_{21}}{\overset{k_{12}}{\rightleftharpoons}} C_2 \underset{k_{32}}{\overset{k_{23}}{\rightleftharpoons}} C_3 \underset{k_{43}}{\overset{k_{34}}{\rightleftharpoons}} C_4 \underset{k_{54}}{\overset{k_{45}}{\rightleftharpoons}} C_5 \;\; k_{56}, k_{65}, O_6, k_{68}, k_{86}, C_8, k_{57}, k_{75}, O_7, k_{78}, k_{87}$$

Model 9

$$C_1 \underset{k_-}{\overset{3k_+}{\rightleftharpoons}} C_2 \underset{2k_-}{\overset{2k_+}{\rightleftharpoons}} C_3 \underset{3k_-}{\overset{k_+}{\rightleftharpoons}} C_4 \underset{\beta}{\overset{\alpha}{\rightleftharpoons}} O_5$$

Model 8-1

$$C_1 \underset{k_{21}}{\overset{k_{12}}{\rightleftharpoons}} C_2 \underset{k_{32}}{\overset{k_{23}}{\rightleftharpoons}} C_3 \underset{k_{43}}{\overset{k_{34}}{\rightleftharpoons}} C_4$$

$$C_3 \underset{k_{53}}{\overset{k_{35}}{\rightleftharpoons}} O_5 \qquad C_4 \underset{k_{64}}{\overset{k_{46}}{\rightleftharpoons}} O_6$$
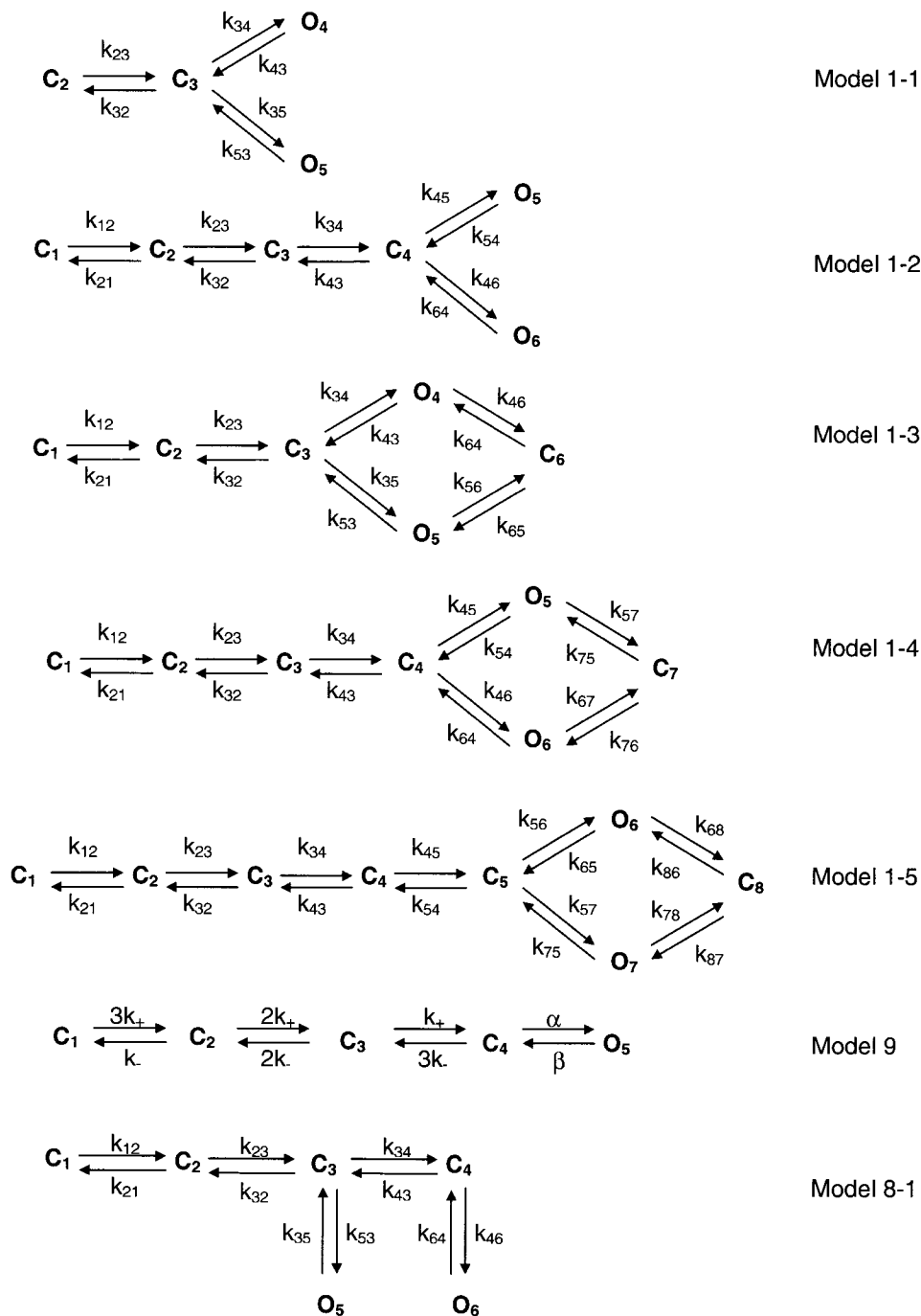
FIGURE 13. Simplified and expanded versions of Model 1 from Fig. 11 (1-1, 1-2, 1-3, and 1-4), and other kinetic models (9 and 8-1) that have been used in the literature.

mental data than that from Model 1-2 (Fig. 13), again suggesting that Model 1-4 is better than Model 1-2.

The dependence of P_o and rate constants on membrane potential. We next tried to determine whether the rate constants were dependent on membrane potential using Model 1-4 (Fig. 13). Fig. 15 A shows the single channel currents activated by 30 μM ATP at voltages from −120 to −80 mV. Fig. 15 B shows the voltage dependence of the mean open and closed times obtained from idealized currents, and Fig. 15 C shows P_o as a function of voltage. The mean open time decreased with depolarization, while the mean closed time increased. The closing and opening rates are both voltage dependent, and the overall effect is to reduce the open probability with depolarization. P_o values calculated from the all-points histogram were slightly larger than those calculated from the idealized currents, suggesting that some short lived events were missed, but the trend was the same; i.e., P_o decreased with depolarization.
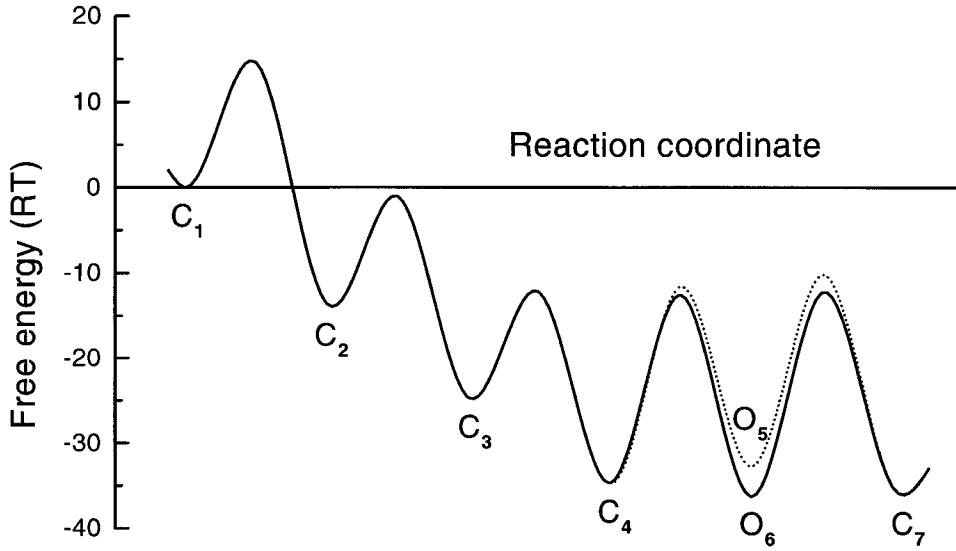
FIGURE 14. Representation of the channel activation pathway in terms of energy barriers and wells based on Model 1-4 (Fig. 13). The free energy landscape of the reaction scheme calculated from the transition rates. The relation between k_{ij} and free energy is defined by the Eyring equation:

$$k_{ij} = \kappa \frac{k_B T}{h} \exp\left(-\frac{G_{ij} - G_i}{RT}\right),$$

(k_{ij}s in this case are the rate constants at -120 mV). κ is the transmission coefficient (assumed to be 1; Hille, 1992), k_B is Boltzmann's constant, h is Planck's constant, and T is the absolute temperature. At 20°C, $k_B T/h$ equals 6.11×10^{12} s^{-1}. G_{ij} is the free energy at the top of the barrier between states i and j, and G_i is the free energy of state i. The free energies are arbitrarily referenced to a solution of 1 M ATP. The use of $k_B T/h$ as the preexponential term of the rates is undoubtedly far off for a macromolecule. However, it is a maximum estimate that will cause the energy barriers to also be maximal estimates. The relationship of the well (state) energies, however, is much more likely to be correct since these energies are determined by ratios of rate constants where the preexponential terms will tend to cancel.

To examine which rate constants vary with voltage, we globally fit the data between -80 and -120 mV with Model 1-4 (Fig. 13). Each rate constant was taken to be of the form:

$$k_{ij}(v) = k_{ij}(0)\exp(-z\delta_{ij}V/k_B T), \quad (14)$$

where $k_{ij}(0)$ is the rate constant at 0 mV, $k_B T$ is Boltzmann's constant times absolute temperature, and $z\delta_{ij}$ is

the effective charge (in a lumped parameter model, a product of the sensing charge and the fraction of the total electric field felt at the location of the sensor). However, this model has many parameters and did not converge [with a detailed balance constraint in loop, there are 30 parameters, including 15 $k_{ij}(0)$ and 15 $z\delta_{ij}$]. We had to apply further constraints to reduce the number of parameters. Since it is presumed that the ATP binding site is located in the extracellular loop (Brake et al., 1994), it is reasonable to assume that it is outside the electric field, and therefore the association and dissociation rates are voltage independent. We fixed them to the values obtained by global fitting based on Model 1-4 (Table VII). The likelihood estimator converged, but with large error limits for k_{ij} and $z\delta_{ij}$ (Table IX). Therefore, we could not make a firm conclusion regarding the voltage dependence for any individual rate constant. However, the predicted P_o using the mean

t a b l e   v i i
Rate Constants Obtained from Global Fitting Based on Models 1-3 and 1-4 (Fig. 13)

Model 1-3		Model 1-4	
Rate constant	Value	Rate constant	Value
		$k_{12}(0)$, (μM^{-1}s^{-1})	3.0 ± 1.1
		k_{21}, (s^{-1})	3.5 ± 2.7
$k_{12}(0)$, (μM^{-1}s^{-1})	19.0 ± 3.8	$k_{23}(0)$, (μM^{-1}s^{-1})	20.3 ± 3.6
k_{21}, (s^{-1})	403 ± 157	k_{32}, (s^{-1})	329 ± 112
$k_{23}(0)$, (μM^{-1}s^{-1})	25.7 ± 3.4	$k_{34}(0)$, (μM^{-1}s^{-1})	24.3 ± 2.9
k_{32}, (s^{-1})	1085 ± 57	k_{43}, (s^{-1})	1098 ± 54
k_{34}, (s^{-1})	1620 ± 61	k_{45}, (s^{-1})	1575 ± 59
k_{43}, (s^{-1})	307 ± 10	k_{54}, (s^{-1})	316 ± 10
k_{35}, (s^{-1})	548 ± 27	k_{46}, (s^{-1})	531 ± 31
k_{53}, (s^{-1})	3509 ± 234	k_{64}, (s^{-1})	3603 ± 233
k_{46}, (s^{-1})	68.4 ± 9.3	k_{57}, (s^{-1})	59.7 ± 9.1
k_{64}, (s^{-1})	184 ± 16	k_{75}, (s^{-1})	178 ± 17
k_{56}, (s^{-1})	1002 ± 159	k_{67}, (s^{-1})	914 ± 163
k_{65}, (s^{-1})	78.2 ± 9.7	k_{76}, (s^{-1})	78.6 ± 11

Single channel currents activated by 5, 10, 15, 20, 30, and 50 μM ATP were used for global fitting. The rate constants near the open states were very close between the two models. Missed events were corrected by imposing a dead time of 0.05 ms.

t a b l e   v i i i
Comparison of Expanded Versions of Model 1 (Fig. 11)

Model	Relative log(Maximum likelihood)	AIC rank	Number of parameters
1-4	+45.4	1	13
1-3	+40.0	2	11
1-2	+5.4	3	10
1	0	4	8

Single channel currents activated by 5, 10, 15, 20, 30, and 50 μM ATP were used for the calculations of maximal likelihoods and AIC ranks. All data were from the same patch. The lowest number of AIC rank is considered best. Detailed balance constraint was applied in the loop of Models 1-3 and 1-4. Missed events were corrected by imposing a dead time of 0.05 ms. (Models 1-2, 1-3, and 1-4 are from Fig. 13.)
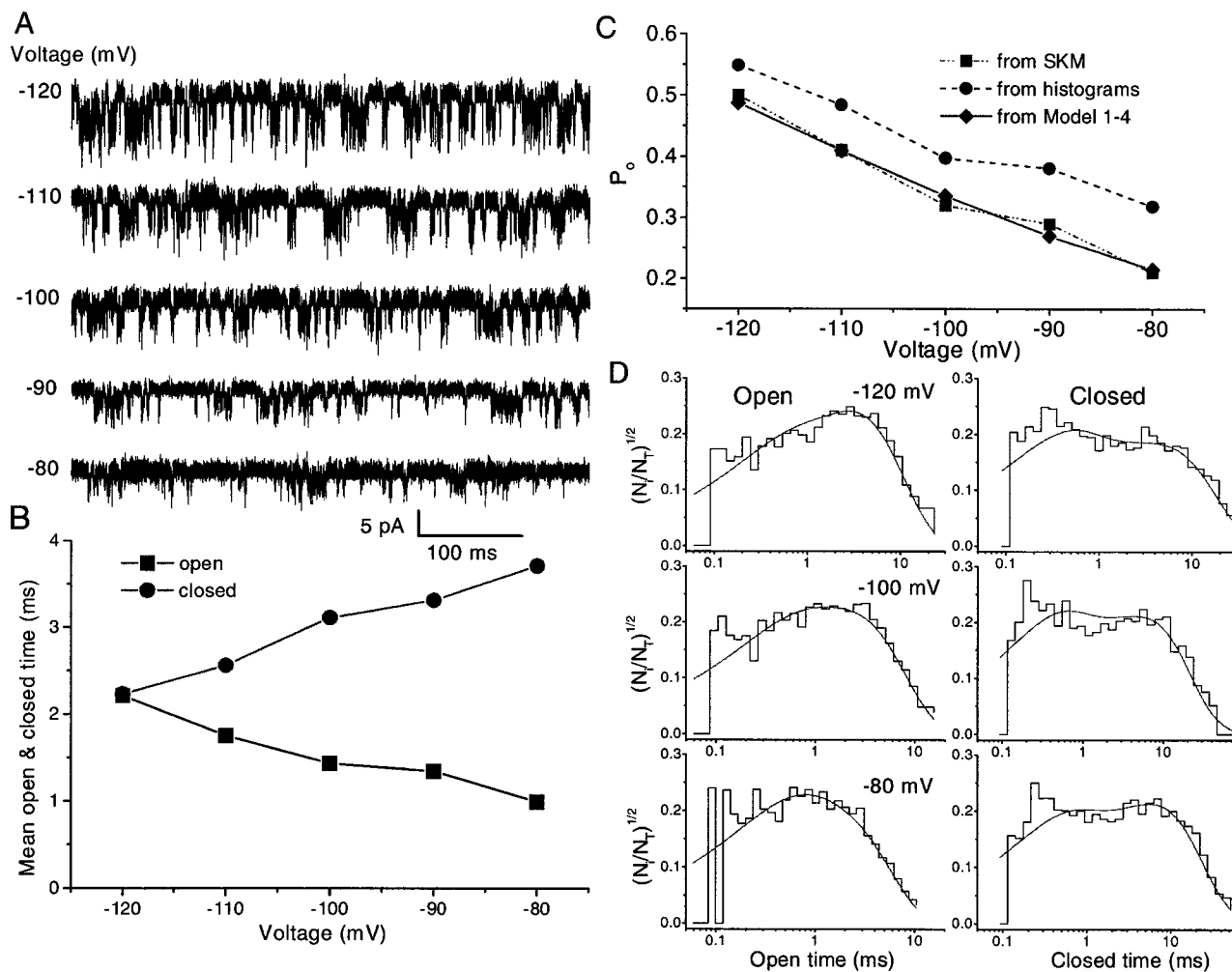
FIGURE 15. The effect of voltage on the single channel currents, mean open and closed times, and P_o. (A) Single-channel currents activated by 30 μM ATP were recorded at different membrane potentials. Other conditions were the same as in Fig. 4. All the current traces in this figure are from the same patch. The currents were idealized for further kinetic analysis after filtering at 5 kHz using a Gaussian digital filter. (B) Mean open and closed times extracted from the idealized currents as a function of voltage. (C) The probability of being open, P_o, as function of voltage calculated from idealized currents (■), all-points histograms (●), and the prediction by Fig. 13, Model 1-4 (◆). P_o from the histogram is slightly larger than that from idealized currents, indicating that some short-lived openings were missed during idealization. P_o predicted by Model 1-4 is close to P_o from idealized currents. (D) The closed and open time histograms at different voltages. The solid lines in the histograms are predicted probability density functions based on Model 1-4. N_i/N_T has the same meaning as in Fig. 10 C.

values of rate constants does decrease with depolarization and is similar to the P_o from idealized currents (Fig. 15 C). Fig. 15 D shows the open and closed interval histogram and the predicted probability densities (solid lines) from the rate constants.

We predicted the shape of the whole cell I–V relationship by combining P_o from outside-out patches and the single channel conductance. The whole cell current I is determined by the product of single channel current, i, the number of channels, n, and the open probability, P_o:

$$I = niP_o. \tag{15}$$

P_o obtained from histograms can be fit with the Boltzmann equation:

$$P_o(V) = P_o(0)\exp(-z\delta V/k_B T), \tag{16}$$

where $P_o(0)$ is P_o at 0 mV, and is equal to 0.11. $z\delta$ is equal to 0.34, indicating that a hyperpolarization of 74 mV is needed for an e-fold increase of P_o. If we presume that the voltage dependence of P_o at different ATP concentrations is the same, we can use this result, together with the dose–response curve (Fig. 4 C), to estimate $P_o(V)$ of a single channel. Multiplying $P_o(V)$ by the single channel current (Fig. 2) predicts the shape

Voltage Dependence of Rate Constants Based on Model 1-4 (Fig. 13)

	$k_{ij}(-120)$	$k_{ij}(0)$	$z\hat{\delta}_{ij}$	mV/e-fold
	s^{-1}	s^{-1}		
$C_4 \to O_5$	344	242 ± 214	0.325 ± 7.85	77
$O_5 \to C_4$	1150	2985 ± 2522	-0.45 ± 7.83	-56
$C_4 \to O_6$	330	376 ± 179	-0.025 ± 45.0	-1000
$O_6 \to C_4$	2166	1189 ± 1926	0.125 ± 7.78	200
$O_5 \to C_7$	25	0.98 ± 3.70	0.675 ± 8.03	37
$C_7 \to O_5$	261	0.02 ± 0.06	1.98 ± 7.70	12.6
$O_6 \to C_7$	214	4303 ± 8698	-0.625 ± 7.8	-137
$C_7 \to O_6$	83	277 ± 566	-0.25 ± 8.03	-100

Rate constants were obtained from global fitting the currents activated by 30 μM ATP from -80 to -120 mV. Each rate constant satisfies the Boltzman equation (Eq. 14). The association and dissociation rates were fixed to the values from different concentration data listed in Table VIII, and were voltage independent. The value of mV/e-fold represents the voltage for an e-fold change in rate constant (negative value implies a depolarization needed for an increase in rate constant).

of the whole-cell I–V relationship. It is close to that predicted by Fig. 13, Model 1-4 (Fig. 3 B).

d i s c u s s i o n

In this study, we have characterized the single channel properties of cloned $P2X_2$ receptor ion channels. The characterization included general gating features, permeation properties, ATP concentration dependence, effects of pH, and kinetic analysis.

Single Channel Current Behavior and Excess Open Channel Noise

The typical single channel Na^+ current has a chord conductance of $\sim$30 pS at -100 mV (Fig. 1). The open channel current shows high frequency, high amplitude flickering with some apparent full closures. Because of the difficulty in resolving the fluctuations comprising this "buzz mode," rather than build a substate model to characterize the open channel behavior, we characterized it as a single conductance with noise. The standard deviation of the excess open channel current is $\sim$30% of the mean. This is much larger than that of the acetylcholine receptor, for example, where the noise is only 2$\sim$5% of the mean (Auerbach and Sachs, 1984; Sigworth, 1985, 1986). The excess noise does not arise from thermal or shot noise nor from the voltage noise of the amplifier (in the worst case, this is $10^{-8}\times$ the thermal noise of the channel; Sigworth, 1985). The fluctuations appear to represent rapid conformational changes that modulate the open channel conductance. Occasionally, we saw relatively long-lived subconductance levels (see Fig. 1 D), but these were too infrequent to be evident in the all-points histograms. We attempted to estimate whether the fluctuations were to a

discrete number of conducting states using a maximum-point likelihood approach. However, we could not find a consistent set of substate amplitudes between records from different patches, although it is clear that the flickers do not represent simple band-limited full closures of the channel. It is possible that there are actually a large number of states better described by a noise rather than a state model. The presence of these rapid fluctuations means that attempts to estimate the unitary channel current with noise analysis are prone to large, bandwidth-dependent errors.

We do not think that the flickers arise from channel block by a diffusible agent, a mechanism that is often seen in other channels. Ca^{2+}-activated K^+ channels can be blocked in a flickery manner by Na^+ (Yellen, 1984), and cardiac Ca^{2+} channels are discretely blocked by divalent ions (Lansman et al., 1986). Since our currents were equally noisy with (Fig. 1 A) and without (Figs. 4 A and 5) extracellular divalent ions, we do not believe that the excess noise comes from the block of divalent ions. ATP is not a candidate for blocking the channels since the mean amplitude and the excess noise are independent of ATP concentration (Fig. 4 A). The voltage dependence of the excess noise is also not significant, suggesting that the flickers do not involve processes that sense the electric field. The simplest interpretation is that the excess noise arises from conformational transitions of the channel itself.

The general features of the cloned $P2X_2$ receptors we have discussed are similar to data recorded from native receptors in rat sensory neurons and PC12 cells (Krishtal et al., 1988; Nakazawa and Hess, 1993). In rat dorsal root ganglion (DRG) cells, single channel currents flickered much more rapidly than in PC12 cells—so rapidly that the lifetime of both states was almost always too short to be resolved by the recording system (Bean et al., 1990). The mean amplitude of the open state with 150 mM extracellular Na^+ was only 0.9 pA at -130 mV with an equivalent chord conductance of 7 pS and no obvious substates. In contrast, we observed a mean single channel current of 3.2 pA, much larger than in the rat DRG cells, with 145 mM extracellular Na^+ at -100 mV with an equivalent mean chord conductance of 32 pS. The true maximum conductance is even larger since the difference in amplitude of the upper 5% of closed and open distributions is 4.3 pA, $\sim$34% larger than the mean current.

I–V Relationship

The single channel I–V relationship of the cloned $P2X_2$ receptors exhibited strong inward rectification (Fig. 2). This result is consistent with the whole cell I–V relationship (Fig. 3) (Brake et al., 1994; Valera et al., 1994). Zhou and Hume (1998) studied the mechanisms of inward rectification of $P2X_2$ receptors. In their data, both

gating and single channel conductance contributed to the inward rectification. They also reported that inward rectification did not require intracellular Mg^{2+} or polyamines, and was present when the same solution was used on both sides of the patch. Our data supports these results. The currents in Fig. 2 were recorded in the presence of 1 mM extracellular Ca^{2+} and Mg^{2+}; however, the single channel current I–V relation showed similar inward rectification when currents were recorded in the absence of divalent cations (data not shown).

Since the mean open and closed times vary with voltage (Fig. 15 B), the opening and closing rate constants are voltage dependent. Although our kinetic analysis was unable make a firm assignment of the voltage dependence to particular rate constants, P_o did decrease with depolarization (Fig. 15 C). The predicted whole cell currents (Fig. 3 B) based on Model 1-4 (Fig. 13) and single channel I–V curve matched reasonably well with the data. These results also suggest that both the instantaneous conductance and voltage-dependent gating contribute to the inward rectification. The dual mechanisms of inward rectification in this receptor are similar to the neuronal nicotinic acetylcholine receptor (Sands and Barish, 1992). The most important feature of the voltage dependence of $P2X_2$ kinetics is that it is minor.

Probability of Being Open

ATP is a potent agonist for cloned P2X receptors, except $P2X_7$, and the receptors are highly selective for ATP over most other adenosine derivatives. Dose–response studies of whole cell currents reveal a Hill coefficient larger than 1 (Brake et al., 1994), suggesting that activation requires more than one agonist. This is reasonable since the channels are composed of multiple homomeric subunits. We studied P_o over a wide range of ATP concentrations with outside-out patches (Fig. 4) and showed that the P_o curve has a Hill coefficient of 2.3, an EC_{50} of 11.2 μM, and a maximum of 0.61. A Hill coefficient of 2.3 suggests that there are at least three binding sites in the receptor. (That the Hill coefficient is only a lower estimate of the stoichiometry is emphasized in Fig. 4 C, where data from a simulation of Model 1-4 [Fig. 13] with three binding steps could be well fit with a Hill coefficient of 1.8). Presumably, the cooperativity arises from the multimeric structure of the channel. Based on refolding studies of the $P2X_2$ extracellular domain ($P2X_2$-ECD), Kim et al. (1997) predicted that the naturally assembled form of $P2X_2$ receptors may be tetrameric. Lewis et al. (1995) found that coexpression of $P2X_2$ and $P2X_3$ can form a new channel type by subunit heteropolymerization, providing further evidence that the P2X receptors are multimers. Recent experiments with chemical cross-linking of $P2X_1$ and $P2X_3$ receptors (Nicke et al., 1998) indicate

that P2X receptor channels are trimeric. Since these results were obtained from native P2X receptors expressed in *Xenopus* oocytes, we expect that they are more representative than the studies on the isolated extracellular domains.

The maximum P_o of $\sim$0.6 indicates that the mean opening rates are slower than the closing rates. Our kinetic analysis based on Model 1-4 (Fig. 13) shows that the two opening rates k_{46} and k_{76} are much slower than corresponding closing rates k_{64} and k_{67}. The opening rate k_{45} is faster than closing rate k_{54}, while the opening rate k_{75} is similar to the closing rate k_{57}, so the overall opening rate is slower than the closing rate.

Affinity of the Pore for Na^+

The theory of independent ion passage predicts that the flux of a permeating ion should increase linearly with the ion concentration (Hille, 1992). However, most channels do not exhibit this behavior due to the competition for binding sites in the channel. Ion flux saturates when the binding–unbinding steps of permeation become rate limiting. This occurs at high ion concentrations when the rate of ion entry approaches the rate of unbinding. Conductances in the $P2X_2$ channels show clear deviations from independence (Fig. 6 A). When the concentration of extracellular NaCl is raised, the single channel conductance saturates. In our data, the mean conductance versus Na^+ concentration was well fit by the Michaelis-Menten (MM) equation, with one binding site, X, in the pore (Scheme II).

$$X + Na^+_{out} \underset{k_{-1}}{\overset{k_1}{\rightleftharpoons}} X\text{-}Na^+ \underset{k_{-2}}{\overset{k_2}{\rightleftharpoons}} X + Na^+_{in}$$
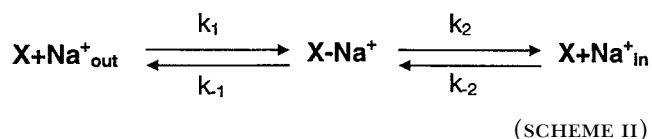
(SCHEME II)

The rate constants are, in general, dependent on membrane potential. We tried to fit our conductance data with Scheme II, but could not obtain a unique set of rate constants: Scheme II is over determined because the data does not have enough distinguishing features. If we assume that at high potentials the reverse flux is negligible, only the two forward rates are necessary and we can obtain solutions. We found that the equilibrium constant K_s is voltage dependent (Fig. 6 B), with the binding site located $\sim$20% of the way through the field relative to the extracellular face. It is interesting to speculate as to where the site may be relative to the primary sequence if one assumes that side chains form the selectivity filter rather than the backbone carbonyls (Doyle et al., 1998). In their study of the ionic pores of $P2X_2$ receptors using the substituted cysteine accessibility method (SCAM), Rassendren et al. (1997a) identified three residues: I328, N333, and T336 in the M2 domain that were located in the outer

vestibule of the pore. Two of these are polar and might be part of a binding site for Na^+. When the channel was open, D349C could be inhibited only by the small, positively charged MTSEA (2-aminoethyl-methanethiosulfonate), but not by MTSET {[2-(trimethylammonium) ethyl]methanethiosulfonate} or MTSES [sodium (2-sulfonatoethyl)methanethiosulfonate], implying that D349 is located near the middle of the channel. D349 is a negatively charged amino acid and is conserved among all seven P2X receptors. It is possible that D349 could be the site of permeant cation binding and is responsible for ionic selectivity.

Cation Selectivity

Our data shows $P2X_2$ is a nonselective cation channel. The ionic selectivity based on the conductance is: $K^+ > Rb^+ > Cs^+ > Na^+ > Li^+$, Eisenman sequence IV (Hille, 1992). This sequence is different from free solution mobility and from the sequence of high field sites. This suggests the pore may be smaller than the nicotinic acetylcholine receptor with an interior having little charge in the selectivity filter. This is consistent with the results from substituted cysteine accessibility method experiments (Rassendren et al., 1997a) where only I328C, N333C, T336C, L338C, and D349C in the M2 domain were accessible to MTS reagents. Only D349 is negatively charged among these residues, and it may not be part of the selectivity filter.

Based on whole cell currents of $P2X_2$ receptors, Brake et al. (1994) reported that the replacement of extracellular Na^+ by K^+ did not affect the reversal potential, suggesting that Na^+ and K^+ have a similar permeability near 0 mV. In our experiments, the currents carried by Na^+ were larger than the currents carried by K^+ at negative potentials. Similar results were reported for PC12 cells (Nakazawa et al., 1990b). The origin of the discrepancy between our results and theirs is masked by the lack of knowledge of the interplay between permeation and gating in the whole cell current. Different ionic environments may change the agonist binding and/or gating. In the nicotinic acetylcholine receptor (Akk and Auerbach, 1996), external monovalent ions compete with agonists for binding, changing the dose–response curves for reasons that have nothing to do with the permeation process itself. If the kinetics of ATP binding and/or gating is different for Na^+ and K^+ in the extracellular solution, P_o will be different, changing the maximum conductance at a fixed agonist concentration.

The excess open channel noise sequence is the same as the cation selectivity (i.e., $K^+ \cong Rb^+ > Cs^+ > Na^+ > Li^+$ (Table I), indicating that it is proportional to the single channel current amplitude, as expected if the noise arises from modulation of the normal flow. If the excess noise arose completely from simple confor-

mational modulation of the pore, all ions would have the same relative selectivity. This is true for all alkali ions with the exception of Li^+, which had $\sim20\%$ smaller relative fluctuations. This suggests a more specific interaction between Li^+ and the channel than for other permeant ions.

pH Potentiation

The sensitivity of cloned $P2X_2$ receptors to ATP was affected by extracellular pH. King reported (King et al., 1996) that with acidification, the ATP dose–response curve of whole cell currents shifted to the left without altering the maximal response. The effective receptor affinity for ATP was enhanced 5–10-fold by acidifying the bath solution (to pH 6.5), but was diminished four- to fivefold in an alkaline solution (pH 8.0). Different P2X receptors have different sensitivities to pH. Unlike $P2X_2$ receptors, $P2X_1$, $P2X_3$, and $P2X_4$ receptors decrease their apparent affinity with acidification (Stoop et al., 1997). Our studies on outside-out patches showed that the mean current increased about an order of magnitude when the extracellular pH changed from 8.3 to 6.8, exhibiting a pK_a of ~7.9 (Fig. 8 B). The Hill coefficient of 2.5 suggests that the channel has at least three binding sites, which is consistent with the stoichiometry study by Nicke et al. (1998). In related experiments, extracellular protons potentiated adenosine binding to A_{2A} receptors, and this effect could be modified by mutagenesis or by chemically altering the strategic residues (Allende et al., 1993). In the extracellular loop of $P2X_2$ receptors, there are 9 histidine residues interspersed between 10 cysteine residues, the latter being conserved throughout the $P2X_{1-7}$ proteins. Both cysteine and histidine residues have been shown to be important for agonist and antagonist binding at the A_1 receptor, which is pH sensitive (Allende et al., 1993). It is reasonable to speculate that these two amino acids may play a similar role in ATP binding to $P2X_2$ receptors. Protonation of the histidine residues may account for the increase in $P2X_2$ current at low pH, but this seems unlikely because diethylpyrocarbonate, which irreversibly denatures histidyl residues, has no effect on the magnitude of the currents (Wildman et al., 1998).

The major effect of pH was on the kinetics of activation. The rate of activation increased as pH decreased (Fig. 8 C), while the deactivation time constant was independent of pH. This suggests that the closing rates and the dissociation rates are not affected by protons. The simplest interpretation of the data is that in acidic environments, the binding site becomes more positive, increasing its affinity for ATP. However, since macroscopic kinetics is a function of all of the rate constants, many of which are not associated with binding, such an interpretation is not reliable.

The single channel current amplitudes at different pH were similar, but the excess open channel noise increased when pH was lowered (Table II). Comparing the single channel currents at different values of pH, as shown in Fig. 9 A, more brief closings can be seen at lower pH. The fluctuations caused by protons are slower than the fluctuations of the intrinsic channel flicker. While these results suggest that protons served as blockers, analysis of the power spectra and single channel kinetics contradict this interpretation. The blocking and unblocking rates were only weakly dependent on proton concentration (see Eq. 13). Power spectral analysis also showed that the corner frequency decreased with an increase in pH, opposite to the prediction for proton block. It appears that the brief closings at low pH are due to conformational changes produced by the titration of several sites.

Kinetics

Preferred model. We used the maximum interval likelihood method to statistically compare kinetic models (Vandenberg and Horn, 1984; Horn, 1987; Qin et al., 1996a). The models were built hierarchically, beginning with one that described the transitions near the open states (Vandenberg and Bezanilla, 1991). The first model we chose (Model 1 or, equivalently, Model 2; Figure 11) had three closed states, C_1, C_2, and C_3, representing unliganded, monoliganded, and biliganded closed states, and two open states O_4 and O_5.

Starting with this model, we expanded to Models 1-2, 1-3, and 1-4 (Fig. 13) to account for the ATP titration data. Comparing Model 1 (Fig. 11) with Model 1-2, and Model 1-3 with Model 1-4, we found that the opening and closing rate constants were surprisingly close (see Tables VI and VII), suggesting that the transitions near the open state were well defined. This result supports our strategy of model development. Among the four models, Model 1-4 had the highest likelihood and AIC rank, and therefore is our preferred model (Table VIII). In this model, there are five closed states, C_1, C_2, C_3, C_4, and C_7, representing unliganded, monoliganded, biliganded, and triliganded closed states, and two open states, O_5 and O_6. The three ATP binding steps require the channel to be at least a trimer. By constraining the ATP association rates to be proportional to concentration, reliable rate constants were obtained from global fitting with this model (Table VII). The predicted probability density functions match reasonably well the open- and closed-time histograms at all concentrations, and the predicted P_o is close to the experimental data so that our final preferred model is Model 1-4.

ATP binding sites and cooperativity. From the results of the basic model (Fig. 11, Model 1) and its expanded versions (Fig. 13, Models 1-2, 1-3, and 1-4), we found that association and dissociation rate constants in-creased as they approached the open states (Table VI and VII). This means that the subunits are not independent and that the association rate for an incoming ATP is increased by the presence of bound ATPs. This trend was consistent among all models examined.

The increase in association rates with consecutive binding is most surprising when one thinks about the opposing electrostatic factors. Bound ATP with a charge of -4 should repel the next incoming ATP (note: the actual valence of bound ATP is not known and is probably less than -4). Since the energy is proportional to the product of the charges, if the sites were independent, the second ATP would be repelled by a resident ATP with an energy proportional to $4*4 = 16$, and the third by $8*4 = 32$. We would thus expect the later binding rates to decrease by more than just the number of available sites. The trend of increasing association rates with occupancy must be caused by conformational changes in the channel that mask the electrostatic contribution. While the increasing rates of dissociation with occupancy fit the predicted electrostatic trend, given the conformational changes associated with binding, this trend may be coincidental. The binding of ATP causes the remaining unoccupied sites to open up in such a manner so as to increase the rates of ATP entry and exit without having a large effect on the equilibrium affinity of the site (Fig. 14).

If the channel were a tetramer, as predicted by Kim et al. (1997), we might add one closed state to the left of C_1 as in Model 1-5 (Fig. 13). We attempted to fit this model, but could not obtain unique rates. This may be because we had insufficient data at very low ATP concentrations, or because the channel really is a trimer (Nicke et al., 1998). The predicted P_o vs. ATP concentration from Model 1-4 (Fig. 13) fits well the P_o, EC_{50}, and Hill coefficient obtained from the dose–response curve (Fig. 4 C), supporting the consistency of the model and the necessity of the last ATP-independent closed state.

Other kinetic models. There have been only a few studies on the kinetics of P2X receptor ion channels based on single channel currents (Krishtal et al., 1988). Kinetic studies using whole cell currents showed that the rise time of current elicited by ATP was strongly concentration dependent, but the decay time was not (Surprenant, 1996). This is in accord with the pH experiments discussed above. There is some variability among reports regarding the rise and fall times. In rat sensory neurons, using fast solution exchange, the rise time was $\sim$10 ms at saturating ATP and the decay time was $\sim$100 ms (Bean et al., 1990). In smooth muscle and cloned $P2X_1$ receptors, the rise time was $\sim$5 ms, while in PC12 cells, cloned $P2X_2$ receptors, and rat superior cervical ganglion (SCG) cells, the rise time was $\sim$25 ms (Surprenant, 1996). In rat SCG cells, nodose, and guinea-

pig coeliac neurons, the latency to the onset of whole cell currents was estimated to be ~0.8–4 ms, and the 10–90% rise time at high ATP concentrations ranged from 5 to 20 ms (Khakh et al., 1995). Since these experiments were done in the whole cell configuration, the rate of rise was likely limited by the speed of the solution exchange around the cells. Hess (1993) reported that the time resolution for solution exchange around a whole cell of this size is 2~10 ms under maximal flow velocities and even slower for lower velocities. With outside-out patches, the rise times can be ~250 μs (Colquhoun et al., 1992). Moreover, because in the whole cell experiments there was no marker for the start of solution exchange, the latency to the onset of the currents could not be estimated accurately.

Preliminary kinetic analysis of single channel currents from rat sensory neurons showed that the distribution of the open times could be approximately fit by two exponentials with time constants of 0.35 and 3.4 ms (Krishtal et al., 1988). The ratio between the fast component amplitude and the slow one varied between patches, with ratios of 47.4:1 to 4.8:1.

Using the rise and fall time constants from whole cell currents at different concentrations of ATP, and based on kinetic models of the ACh receptor channel, Bean (1990) proposed a linear kinetic model with independent subunits for ATP activation (Fig. 13, Model 9). The association and dissociation rate constants $k_+ = 1.2 \times 10^7$ M^{-1}s^{-1} and $k_- = 4$ s^{-1} were chosen so that the simulations mimicked the kinetics seen in the bullfrog sensory neurons. Agreement between the model and the data suggested that the ATP binding sites could be independent.

We applied the independent binding site assumption to Model 1-2; i.e., $k_{34} = 1/2k_{23} = 1/3k_{12} = 1/3k_{10} = k_+$, and $k_{21} = 1/2k_{32} = 1/3k_{43} = k_-$. Although the estimation converged, the likelihood was much lower than our favored models. We also fit our data with Bean's (1990) model, which has only one open state (Fig. 13, Model 9), and again the fits were poor.

In other ligand-gated channels, such as the Ca^{2+}-activated potassium channel and ACh receptors (Magleby and Song, 1992; Auerbach et al., 1996), partially liganded channels can open. To explore whether these states were visible in our data, we compared the maximum likelihood of Model 8-1 (Fig. 13) that has partially liganded openings with Model 1-2 (Fig. 13). Global fitting of Model 8-1 with data from 5, 10, 15, 20, 30, and 50 μM ATP produced a maximum likelihood 664 units lower than Model 1-2, suggesting the model is $e^{664}\times$ less likely to produce the data. Apparently, P2X$_2$ channels do not open for a significant fraction of time in partially liganded states.

In summary, Model 1-4 (Fig. 13) can well represent the channel gating processes. It is adequate to explain the behavior across concentration and is physically reasonable. Fig. 14 shows the calculated free energy barriers and wells at −120 mV referenced to 1 M ATP. The energies were calculated from the rate constants assuming an Eyring model. The free energies of all wells decreased with the reaction coordinate. State C$_4$ could go to either open state O$_5$ or O$_6$ with state O$_5$ being slightly more stable. O$_5$ and O$_6$ go to the same closed state C$_7$ that is the most stable in the reaction pathway.

Voltage dependence of P_o and rate constants. Although P_o is not strongly dependent on membrane potential, it did decrease with depolarization (Fig. 15 C), indicating that some of the rate constants are voltage dependent. To reduce the free parameters, we limited the voltage sensitivity to only the rate constants in the final loop and ended up with very large errors limits for $k_{ij}(0)$ and $z\delta_{ij}$. We have no confidence in the voltage dependence of any of the individual rate constants. Data from a wider voltage range will be required to adequately address this question.

Despite the wide error limits, by lumping the kinetics into an equilibrium model to predict the probabilities of occupancy, the predicted P_o and whole cell currents calculated from the mean values of $k_{ij}(0)$ and $z\delta_{ij}$ were consistent with those obtained by idealization (Fig. 15 C) and with experimental data (Fig. 3 B). The probability density functions match reasonably well with duration histograms (Fig. 15 D).

In conclusion, the currently optimal model, Model 1-4 (Fig. 13), can be summarized as follows: (a) the channel proceeds through three ATP binding steps before opening; (b) the three ATP binding sites are not independent, but positively cooperative; (c) There are two open states, which connect to a common ATP-independent closed state; (d) activation and deactivation proceed along the same pathway; and (e) channels only open after being fully liganded.

r e f e r e n c e s

Akk, G., and A. Auerbach. 1996. Inorganic, monovalent cations compete with agonists for the transmitter binding site of nicotinic acetylcholine receptors. *Biophys. J.* 70:2652–2658.

Allende, G., V. Casado, J. Mallol, R. Franco, C. Lluis, and E.I. Canela. 1993. Role of histidine residues in agonist and antagonist binding sites of A1 adenosine receptor. *J. Neurochem.* 60:1525–1533.

Auerbach, A., and F. Sachs. 1984. Single-channel currents from acetylcholine receptors in embryonic chick muscle. Kinetic and conductance properties of gaps within bursts. *Biophys. J.* 45:187–198.

Auerbach, A., W. Sigurdson, J. Chen, and G. Akk. 1996. Voltage dependence of mouse acetylcholine receptor gating: different charge movements in di-, mono-, and unliganded receptors. *J. Physiol. (Camb.).* 494:155–170.

Barry, P.H., and J.W. Lynch. 1991. Liquid junction potentials and small cell effects in patch-clamp analysis. [Published erratum appears in *J. Membr. Biol.* 1992. 125:286.] *J. Membr. Biol.* 121:101–117.

Bean, B.P. 1990. ATP-activated channels in rat and bullfrog sensory neurons: concentration dependence and kinetics. *J. Neurosci.* 10:1–10.

Bean, B.P. 1992. Pharmacology and electrophysiology of ATP-activated ion channels. *Trends Pharmacol. Sci.* 13:87–90.

Bean, B.P., C.A. Williams, and P.W. Ceelen. 1990. ATP-activated channels in rat and bullfrog sensory neurons: current–voltage relation and single-channel behavior. *J. Neurosci.* 10:11–19.

Bo, X., Y. Zhang, M. Nassar, G. Burnstock, and R. Schoepfer. 1995. A P2X purinoceptor cDNA conferring a novel pharmacological profile. *FEBS Lett.* 375:129–133.

Brake, A.J., M.J. Wagenbach, and D. Julius. 1994. New structural motif for ligand-gated ion channels defined by an ionotropic ATP receptor. *Nature.* 371:519–523.

Bretschneider, F., M. Klapperstuck, M. Lohn, and F. Markwardt. 1995. Nonselective cationic currents elicited by extracellular ATP in human B-lymphocytes. *Pflügers Arch.* 429:691–698.

Buell, G., C. Lewis, G. Collo, R.A. North, and A. Surprenant. 1996. An antagonist-insensitive P2X receptor expressed in epithelia and brain. *EMBO (Eur. Mol. Biol. Organ.) J.* 15:55–62.

Capiod, T. 1998. ATP-activated cation currents in single guinea-pig hepatocytes. *J. Physiol. (Camb.).* 507:795–805.

Chen, C.C., A.N. Akopian, L. Sivilotti, D. Colquhoun, G. Burnstock, and J.N. Wood. 1995. A P2X purinoceptor expressed by a subset of sensory neurons. *Nature.* 377:428–431.

Chung, S.H., J.B. Moore, L.G. Xia, L.S. Premkumar, and P.W. Gage. 1990. Characterization of single channel currents using digital signal processing techniques based on Hidden Markov Models. *Philos. Trans. R. Soc. Lond. B Biol. Sci.* 329:265–285.

Collo, G., R.A. North, E. Kawashima, E. Merlo-Pich, Neidhart, A. Surprenant, and G. Buell. 1996. Cloning OF P2X5 and P2X6 receptors and the distribution and properties of an extended family of ATP-gated ion channels. *J. Neurosci.* 16:2495–2507.

Colquhoun, D., P. Jonas, and B. Sakmann. 1992. Action of brief pulses of glutamate on AMPA/kainate receptors in patches from different neurones of rat hippocampal slices. *J. Physiol. (Camb.).* 458:261–287.

Defelice, L. 1981. Introduction to Membrane Noise. Plenum Publishing Corp. New York. 231–329.

Doyle, D.A., J.M. Cabral, R.A. Pfuetzner, A. Kuo, J.M. Gulbis, S.L. Cohen, B.T. Chait, and R. MacKinnon. 1998. The structure of the potassium channel: molecular basis of K^+ conduction and selectivity. *Science.* 280:69–77.

Evans, R.J. 1996. Single channel properties of ATP-gated cation channels (P2X receptors) heterologously expressed in Chinese hamster ovary cells. *Neurosci. Lett.* 212:212–214.

Friel, D.D. 1988. An ATP-sensitive conductance in single smooth muscle cells from the rat vas deferens. *J. Physiol. (Camb.).* 401:361–380.

Hamill, O.P., A. Marty, E. Neher, B. Sakmann, and F.J. Sigworth. 1981. Improved patch-clamp techniques for high-resolution current recording from cells and cell-free membrane patches. *Pflügers Arch.* 391:85–100.

Hess, G.P. 1993. Determination of the chemical mechanism of neurotransmitter receptor-mediated reactions by rapid chemical kinetic techniques. *Biochemistry.* 32:989–1000.

Hille, B. 1992. Ionic Channels of Excitable Membranes. 2nd edition. Sinauer Associates Inc., Sunderland, MA. 362–389.

Horn, R. 1987. Statistical methods for model discrimination. Applications to gating kinetics and permeation of the acetylcholine receptor channel. *Biophys. J.* 51:255–263.

Khakh, B.S., P.P. Humphrey, and A. Surprenant. 1995. Electrophysiological properties of P2X-purinoceptors in rat superior cervical, nodose and guinea-pig coeliac neurones. *J. Physiol. (Camb.).* 484:385–395.

Kim, M., O.J. Yoo, and S. Choe. 1997. Molecular assembly of the extracellular domain of P2X2, an ATP-gated ion channel. *Biochem. Biophys. Res. Commun.* 240:618–622.

King, B.F., S.S. Wildman, L.E. Ziganshina, J. Pintor, and G. Burnstock. 1997. Effects of extracellular pH on agonism and antagonism at a recombinant P2X2 receptor. *Br. J. Pharmacol.* 121:1445–1453.

King, B.F., L.E. Ziganshina, J. Pintor, and G. Burnstock. 1996. Full sensitivity of P2X2 purinoceptor to ATP revealed by changing extracellular pH. *Br. J. Pharmacol.* 117:1371–1373.

Krishtal, O.A., S.M. Marchenko, and A.G. Obukhov. 1988. Cationic channels activated by extracellular ATP in rat sensory neurons. *Neuroscience.* 27:995–1000.

Lansman, J.B., P. Hess, and R.W. Tsien. 1986. Blockade of current through single calcium channels by Cd^{2+}, Mg^{2+}, and Ca^{2+}. Voltage and concentration dependence of calcium entry into the pore. *J. Gen. Physiol.* 88:321–347.

Lewis, C., S. Neidhart, C. Holy, R.A. North, G. Buell, and A. Surprenant. 1995. Coexpression of P2X2 and P2X3 receptor subunits can account for ATP-gated currents in sensory neurons. *Nature.* 377:432–435.

Li, C., R.W. Peoples, and F.F. Weight. 1996. Acid pH augments excitatory action of ATP on a dissociated mammalian sensory neuron. *Neuroreport.* 7:2151–2154.

Li, C., R.W. Peoples, and F.F. Weight. 1997. Enhancement of ATP-activated current by protons in dorsal root ganglion neurons. *Pflügers Arch.* 433:446–454.

Magleby, K.L., and L. Song. 1992. Dependency plots suggest the kinetic structure of ion channels. *Proc. R. Soc. Lond. B Biol. Sci.* 249:133–142.

McQueen, D.S., S.M. Bond, C. Moores, I. Chessell, P.P. Humphrey, and E. Dowd. 1998. Activation of P2X receptors for adenosine triphosphate evokes cardiorespiratory reflexes in anaesthetized rats. *J. Physiol. (Camb.).* 507:843–855.

Nakazawa, K., K. Fujimori, A. Takanaka, and K. Inoue. 1990a. ATP-induced current in isolated outer hair cells of guinea pig cochlea. *J. Neurophysiol. (Bethesda).* 63:1068–1074.

Nakazawa, K., K. Fujimori, A. Takanaka, and K. Inoue. 1990b. An ATP-activated conductance in pheochromocytoma cells and its suppression by extracellular calcium. *J. Physiol. (Camb.).* 428:257–272.

Nakazawa, K., and P. Hess. 1993. Block by calcium of ATP-activated channels in pheochromocytoma cells. *J. Gen. Physiol.* 101:377–392.

Nakazawa, K., K. Inoue, K. Fujimori, and A. Takanaka. 1991. Effects

of ATP antagonists on purinoceptor-operated inward currents in rat phaeochromocytoma cells. *Pflügers Arch.* 418:214–219.

Nicke, A., H.G. Baumert, J. Rettinger, A. Eichele, Lambrecht, E. Mutschler, and G. Schmalzing. 1998. P2X1 and P2X3 receptors form stable trimers: a novel structural motif of ligand-gated ion channels. *EMBO (Eur. Mol. Biol. Organ.) J.* 17:3016–3028.

North, R.A. 1996. Families of ion channels with two hydrophobic segments. *Curr. Opin. Cell Biol.* 8:474–483.

Qin, F., A. Auerbach, and F. Sachs. 1996a. Estimating single-channel kinetic parameters from idealized patch-clamp data containing missed events. *Biophys. J.* 70:264–280.

Qin, F., A. Auerbach, and F. Sachs. 1996b. Idealization of single-channel currents using the segmental K-mean method. *Biophys. J.* 72:A227

Rassendren, F., G. Buell, A. Newbolt, R.A. North, and A. Surprenant. 1997a. Identification of amino acid residues contributing to the pore of a P2X receptor. *EMBO (Eur. Mol. Biol. Organ.) J.* 16:3446–3454.

Rassendren, F., G.N. Buell, C. Virginio, G. Collo, R.A. North, and A. Surprenant. 1997b. The permeabilizing ATP receptor, P2X7. Cloning and expression of a human cDNA. *J. Biol. Chem.* 272: 5482–5486.

Rudy, B., and L. Iverson. 1992. Methods in Enzymology. Vol. 207. Academic Press, Inc., San Diego, CA. 266–279.

Sands, S.B., and M.E. Barish. 1992. Neuronal nicotinic acetylcholine receptor currents in phaeochromocytoma (PC12) cells: dual mechanisms of rectification. *J. Physiol. (Camb.).* 447:467–487.

Seguela, P., A. Haghighi, J.J. Soghomonian, and E. Cooper. 1996. A novel neuronal P2X ATP receptor ion channel with widespread distribution in the brain. *J. Neurosci.* 16:448–455.

Sigworth, F.J. 1985. Open channel noise. I. Noise in acetylcholine receptor currents suggests conformational fluctuations. *Biophys. J.* 47:709–720.

Sigworth, F.J. 1986. Open channel noise. II. A test for coupling between current fluctuations and conformational transitions in the acetylcholine receptor. *Biophys. J.* 49:1041–1046.

Sigworth, F.J., and S.M. Sine. 1987. Data transformations for improved display and fitting of single-channel dwell time histograms. *Biophys. J.* 52:1047–1054.

Sivilotti, L.G., D.K. McNeil, T.M. Lewis, M.A. Nassar, R. Schoepfer, and D. Colquhoun. 1997. Recombinant nicotinic receptors, expressed in *Xenopus* oocytes, do not resemble native rat sympathetic ganglion receptors in single-channel behaviour. *J. Physiol.*

(Camb.). 500:123–138.

Soto, F., M. Garcia-Guzman, J.M. Gomez-Hernandez, M. Hollmann, C. Karschin, and W. Stühmer. 1996. P2X4: an ATP-activated ionotropic receptor cloned from rat brain. *Proc. Natl. Acad. Sci. USA.* 93:3684–3688.

Stoop, R., A. Surprenant, and R.A. North. 1997. Different sensitivities to pH of ATP-induced currents at four cloned P2X receptors. *J. Neurophysiol.* 78:1837–1840.

Surprenant, A. 1996. Functional properties of native and cloned P2X receptors. *Ciba Found. Symp.* 198:208–219.

Surprenant, A., F. Rassendren, E. Kawashima, R.A. North, and G. Buell. 1996. The cytolytic P2Z receptor for extracellular ATP identified as a P2X receptor (P2X7). *Science.* 272:735–738.

Ugur, M., R.M. Drummond, H. Zou, P. Sheng, J.J. Singer, and J.V. Walsh, Jr. 1997. An ATP-gated cation channel with some P2Z-like characteristics in gastric smooth muscle cells of toad. *J. Physiol. (Camb.).* 498:427–442.

Valera, S., N. Hussy, R.J. Evans, N. Adami, R.A. North, A. Surprenant, and G. Buell. 1994. A new class of ligand-gated ion channel defined by P2X receptor for extracellular ATP. *Nature.* 371:516–519.

Vandenberg, C.A., and F. Bezanilla. 1991. Single-channel, macroscopic, and gating currents from sodium channels in the squid giant axon. *Biophys. J.* 60:1499–1510.

Vandenberg, C.A., and R. Horn. 1984. Inactivation viewed through single sodium channels. *J. Gen. Physiol.* 84:535–564.

Walz, W., G. Gimpl, C. Ohlemeyer, and H. Kettenmann. 1994. Extracellular ATP-induced currents in astrocytes: involvement of a cation channel. *J. Neurosci. Res.* 38:12–18.

Wang, C.Z., N. Namba, T. Gonoi, N. Inagaki, and S. Seino. 1996. Cloning and pharmacological characterization of a fourth P2X receptor subtype widely expressed in brain and peripheral tissues including various endocrine tissues. *Biochem. Biophys. Res. Commun.* 220:196–202.

Wildman, S.S., B.F. King, and G. Burnstock. 1998. Zn^{2+} modulation of ATP-responses at recombinant P2X2 receptors and its dependence on extracellular pH. *Br. J. Pharmacol.* 123:1214–1220.

Yellen, G. 1984. Ionic permeation and blockade in Ca^{2+}-activated K^+ channels of bovine chromaffin cells. *J. Gen. Physiol.* 84:157–186.

Zhou, Z., and R.I. Hume. 1998. Two mechanisms for inward rectification of current flow through the purinoceptor P2X2 class of ATP-gated channels. *J. Physiol. (Camb.).* 507:353–364.